AIAA JOURNAL
Vol. 59, No. 7, July 2021

Automatic Transition Prediction in a Navier–Stokes Solver Using Linear Stability Theory

Jan-Sören Fischer* and Bambang I. Soemarwoto†
Netherlands Aerospace Centre (NLR), 1059 CM Amsterdam, The Netherlands
and
Edwin T. A. van der Weide‡
University of Twente, 7522 NB Enschede, The Netherlands

https://doi.org/10.2514/1.J059910

A structured Reynolds-averaged Navier–Stokes solver is directly coupled to a linear stability theory (LST) solver to include the effect of laminar–turbulent transition in the flow simulations. The flowfield variables of the flow solver are used to both find streamlines along which transition can be predicted and to provide the LST code with the required boundary-layer profiles. Instabilities included in the analysis are of the Tollmien–Schlichting and crossflow nature relevant to high-Reynolds-number flows in low turbulence environments. The coupling is fully automated and can therefore be used efficiently in the analysis and design of geometries with external flows. The Technical University of Braunschweig's sickle wing with spanwise-varying crossflow and the natural laminar flow version of the Common Research Model are simulated under various conditions. Applications to these relevant three-dimensional test cases showcase the capability of the method to model the real flow physics. Advantages and challenges of the approach with regard to future design endeavors are discussed.

Nomenclature

A = amplification
C_d = drag coefficient
C_f = friction coefficient
C_l = lift coefficient
C_p = pressure coefficient
b = span, m
c = chord, m
H_{12} = shape factor; δ^*/θ
H_{32} = energy shape factor; δ_3/θ
$\mathbf{k}$ = wave number vector
l = length
M = Mach number
N = N factor
p = pressure, Pa
Re = Reynolds number
s = arc length, m
T = temperature, K
Tu = turbulence intensity, %
t = time, s
$\mathbf{u}$ = velocity vector, m/s
u, v, w = velocities in the x, y, and z directions, m/s
α = angle of attack, deg; wave number in x
β = wave number in y
γ = intermittency
δ = boundary-layer thickness, m
δ_3 = energy thickness, m
δ^* = displacement thickness, m
θ = momentum thickness, m
λ = Wavelength, m
μ_t = eddy viscosity, $\mathrm{Pa} \cdot \mathrm{s}$
ξ, ζ = under-relaxation factors
ρ = density, $\mathrm{kg/m^3}$
ϕ = sweep angle, deg
ψ = wave angle, deg
ω = frequency, $\mathrm{s^{-1}}$

Subscripts

CF = crossflow
g = group
e = boundary-layer edge
low = lower
MAC = mean aerodynamic chord
sep = separation
TS = Tollmien–Schlichting
tm = turbulence model
tr = transition
up = upper
∞ = freestream

I. Introduction

LAMINAR–TURBULENT transition plays a major role in the characteristics of wall-bounded flows. Especially for the computational determination of aircraft drag, an accurate prediction of the transition location is essential because friction drag accounts for roughly half of the total drag of a modern airliner during cruise flight. However, it is difficult to achieve. Flow models with intrinsic transition prediction like direct numerical simulations or large-eddy simulations are computationally too expensive for practical application in design activities for high-Reynolds-number flows around wings. Lower-fidelity models like Reynolds-averaged Navier–Stokes (RANS) simulations are computationally cheaper but are, by themselves, incapable of predicting the transition location. An additional transition prediction model is needed to determine laminar–turbulent transition. As RANS remains the predominant analysis and design tool for industrial applications in the foreseeable future, the combined models can provide an affordable, robust, and yet accurate prediction of transitional flows.

Transition prediction approaches currently existing in conjunction with non-turbulence-resolving computational fluid dynamics (CFD) can be classified into methods based on 1) analytical criteria, 2) database methods, 3) correlation-based transport equations, and 4) stability analysis. The first three methods have all successfully been implemented in

---

Received 22 June 2020; revision received 28 October 2020; accepted for publication 19 December 2020; published online 20 May 2021.

*Ph.D. Student, Department of Flight Physics and Loads, Anthony Fokkerweg 2. Student Member AIAA.

†Senior Research Scientist, Department of Flight Physics and Loads, Anthony Fokkerweg 2.

‡Associate Professor, Department of Mechanical Engineering, Drienerlolaan 5. Senior Member AIAA.

existing CFD codes and were applied to flows ranging from academic test cases to full aircraft configurations [1–4]. The easier implementation and expectedly modest computational effort offer strong arguments, especially for use in (unstructured) industrial flow solvers. There remain a number of disadvantages to these methods, however, that convince the authors that stability theory, at this stage, remains an attractive transition prediction method, although it may require larger implementation efforts and computational resources. A first challenge is, in light of design efforts, to directly link the resulting transition locations to the underlying physical transitional flow phenomena. Additionally, the reliance on the databases and correlations always poses a question on the applicability of the models to the flow conditions under consideration that are not necessarily captured well by the underlying dataset. Stability theory with its direct physical foundation for determining transition does not suffer from these issues, such that the additional computational and implementation efforts are regarded as worth the investment.

Existing approaches using stability theory in conjunction with RANS for three-dimensional geometries in an automated manner include that of Krumbein et al. [5], Krimmelbein and Radespiel [6], Krumbein et al. [7,8], or Shi et al. [9], who coupled unstructured CFD codes with linear stability solvers with optional use of an intermediate laminar boundary-layer (BL) code to obtain accurate boundary-layer profiles from the RANS pressure distributions. Furthermore, Campbell and Lynde [10] showed a coupling of an unstructured code with different stability solvers for a laminar wing design framework. Kosarev et al. [11] demonstrated the application of a coupling between RANS and a parabolized stability equation solver with automated input generation using an LST code.

In this work, a transition prediction technique implemented in the Netherlands Aerospace Centre/NLR's (NLR's) structured ENSOLV code is described. It is shown how linear stability theory (LST) is used together with a steady RANS method, analyzing amplified disturbances along integration paths on aircraft surfaces in order to determine the susceptibility of the laminar boundary layer to natural transition. A transition line is found using the e^N approach [12,13] for different transition mechanisms. The required convergence criteria and grid densities are identified to accurately predict transition.

The application to two test cases, the Technical University of Braunschweig's (TU Braunschweig's) sickle wing and NASA's Common Research Model natural laminar flow (CRM-NLF) wing, demonstrates the capabilities and limitations of the implemented method. Furthermore, the LST analysis allows for a detailed analysis of the transition mechanisms.

II. Transitional Flow Modeling

The flow simulations are performed using a RANS-based modeling approach. Because this model in its original form is fully turbulent, the laminar and transitional regions must be modeled differently to include transition effects.

A. Flow Solver

The simulations in this work were conducted with the ENSOLV code, which is part of the CFD system ENFLOW, developed in-house at NLR [14,15]. ENSOLV is a structured multiblock RANS solver that employs a cell-centered finite volume method for the spatial discretization. Use is made of a Jameson-type artificial dissipation scheme blending second- and fourth-order terms [16,17]. In boundary-layer regions, a matrix form of the artificial dissipation is applied to minimize numerical diffusion, and therefore to improve numerical accuracy. In the present work, an explicit algebraic Reynolds-stress model [18] based on the turbulent–nonturbulent $k-\omega$ model was used, removing the dependency on the freestream turbulence level [19].

Time-accurate integration is carried out using a dual-time-stepping scheme employing the Runge–Kutta method for the relaxation in pseudotime; the latter of which is also used to obtain the steady-state solution of the RANS equations. To accelerate the convergence, the discretized equations are solved using a full approximation storage multigrid scheme. The computations were carried out on NLR's high-performance computing facilities, for which the solver has been optimized with a hybrid MPI–OpenMP parallelization strategy.

B. Transitional Flow Simulation

To simulate the transitional flow, the domain around the aerodynamic body of consideration is divided into two regions: a laminar one and a turbulent one. The laminar region upstream of the transition line is forced to have zero eddy viscosity. Downstream of the transition line, the eddy viscosity is ramped up for a correct prediction of the turbulent flowfield. The ramping up of the eddy viscosity can be regarded as the transition region modeling, and it is called intermittency γ. It is defined as the ratio of applied eddy viscosity over eddy viscosity as provided by the turbulence model. Due to the high Reynolds numbers under consideration, the transition region is small compared to the streamwise lengths of the surface on which transition occurs. Therefore, no sophisticated models to determine the transition length are employed apart from ensuring a smooth ramp-up function is used for reasons of numerical stability:

$$\gamma = \frac{\mu_t}{\mu_{t,\mathrm{tm}}} = 1 - \exp\left(\frac{2.78 \cdot (\Delta x)^2}{l_{\mathrm{tr}}^2}\right) \tag{1}$$

In the present work, the transition length l_{tr} is defined as the total length in the streamwise direction of the four cells downstream of the transition location. This ensures a smooth but fast ramp up of the eddy viscosity at the transition location. Δx is defined as the streamwise distance from the transition line. If, in future work, more interest in the transition region modeling arises, empirical models for the approximation of the transition length exist [20].

III. Transition Prediction

Within the realm of stability analysis methods, its simplest form of the linear stability theory is still the most prominent one [5]. Simplifications include the reduction to linear instabilities only, a parallel flow assumption, and often the neglection of curvature terms. The more sophisticated linearized parabolized stability equations include nonparallel effects but have not resulted in a significant reduction in the error for N-factor computations. Consequently, they have not managed to gain as much popularity as the LST. The nonlinear stability equations are a powerful tool to analyze the growth of specific instabilities. The computational cost related to solving these equations and the need to specify initial mode amplitudes, however, make it unfeasible to use them for general transition prediction in CFD codes [21].

Linear stability theory provides a physics-based means of assessing the stability of boundary layers and has its origins in the early 20th century. Since researchers started to numerically apply this approach in the 1960s, it has shown its suitability to determine transition locations for many applications [21–23]. Especially for applications where nonlinear transition mechanisms play a minor role in the determination of the transition location, it is an accurate analysis tool. The flows considered in this work feature high Reynolds numbers of $Re = \mathcal{O}(10^6)$ or higher and low freestream turbulence levels of $Tu = \mathcal{O}(0.1\%)$. Transition is therefore not expected to occur due to bypass transition. Instead, streamwise Tollmien–Schlichting (TS) and stationary crossflow (CF) instabilities dominate the transition phenomena [24]. Previous work has also shown that in the flows under consideration, the exponential growth of instabilities can be accurately captured with LST and secondary instabilities lead to a very sudden breakup into turbulence once a certain threshold of the exponential amplification is reached. As such, the nonlinear instabilities play an important physical role in the actual transition to turbulence, but they hardly affect the transition location itself.

In the present paper, an improved NLR version (COSALX [25]) of the COSAL stability code developed by Malik [26] was used. Changes to Malik's original version include the inclusion of additional N-integration strategies, an automatic grid refinement, and a bypass option for the global eigenvalue search to speed up the computations. The LST code solves the compressible three-dimensional stability equations. These are derived from the three-dimensional compressible Navier–Stokes (NS) equations by linearization of the flow variable fluctuations around the mean flow. Additionally, the parallel flow assumption is made, and normal modes are assumed for the instabilities as shown in Eq. (2):

$$[u, v, w, p, \rho, T] = [\hat{u}, \hat{v}, \hat{w}, \hat{p}, \hat{\rho}, \hat{T}]e^{i(\alpha x + \beta z - \omega t)} \tag{2}$$

where $\omega = \omega(\alpha, \beta)$. Here, α and β are the x and z components of the wave number vector $\boldsymbol{k}$ of the mode, and ω is its frequency. The wave angle of the wave with the x axis is $\psi_w = \tan^{-1}(\beta/\alpha)$. Any complex component of these variables will change the propagation of the wave. The x direction follows the integration path of the instability, y is the wall-normal direction, and z is defined as the crossflow direction parallel to the wall and normal to the integration path. The result of substituting these modes into the disturbance equations is an eigenvalue problem:

$$A \cdot D^2\boldsymbol{\phi} + B \cdot D\boldsymbol{\phi} + C\boldsymbol{\phi} = 0 \tag{3}$$

where A, B, and C are complex matrices; D denotes differentiation with respect to y; and $\boldsymbol{\phi} = [\alpha\hat{u} + \beta\hat{w}, \hat{v}, \hat{p}, \hat{T}, \alpha\hat{w} - \beta\hat{u}]^T$. The interested reader is referred to Ref. [27] for a more complete description of the equations and the solution procedure that is outlined in the following. COSALX uses temporal theory to solve the problem such that disturbances are assumed to only grow in time, leading to α and β being real and ω being complex. The eigenvalue problem is discretized with a second-order-accurate finite difference formulation. A global eigenvalue search is performed on a coarse mesh using a complex LR algorithm to find an initial guess of the eigenvalues. A more accurate local search is then performed on a finer mesh using a block LU factorization with inverse Rayleigh iterations to solve the problem.

Using Gaster's transformation [28], the spatial amplification of the wave amplitude in the direction of the group velocity $\boldsymbol{v_g} = [\partial\omega/\partial\alpha, \partial\omega/\partial\beta]$ is related to the imaginary part of the frequency according to Eq. (4):

$$\frac{1}{A} \cdot \frac{dA}{dx} = -\alpha_i \approx \frac{\omega_i}{|\boldsymbol{v_g}|} \tag{4}$$

If ω_i is positive the mode is amplified. If ω_i is negative the mode is damped. The amplification factor (N factor) can now be integrated along the integration path using

$$N = \ln\left(\frac{A}{A_0}\right) = \int_{x_0}^{x} \frac{\omega_i}{v_g}\,\mathrm{d}x \tag{5}$$

Transition is assumed to occur where N exceeds a certain value: the limiting N factor. The limiting N factor is primarily dependent on the freestream turbulence level as shown by Mack's relation [22] for TS instabilities [Eq. (6)] derived from experimental data:

$$N_{\mathrm{TS,tr}} = -8.43 - 2.4\,\ln(Tu) \tag{6}$$

The propagation of a disturbance is determined by multiple, so far undefined parameters. Additional assumptions on the mode's frequency, wavelength, and orientation are required to define how the local N factors are integrated along a streamline. Various integration strategies are available in COSALX. In this work, two different sets of assumptions are used to analyze streamwise N_{TS} and crossflow N_{CF} instabilities, respectively. For streamwise instabilities, a certain frequency and a fixed wave orientation are set; and an initial wavelength is provided that is allowed to change along the integration path. This essentially assumes that the most amplified mode is perfectly aligned with the integration path, which is not necessarily the case, but the variation of the N factor around this direction was found to be small for the conditions under consideration in this work [29]. Additionally, no problems with pathological cases were encountered in the analyzed cases as described by Arnal [30]. For crossflow instabilities, a fixed wavelength is prescribed with a zero frequency, resulting in a stationary crossflow wave [21,29]. The wave orientation is varied along the path to find the most unstable mode. With those two N factors determined along an integration path, a two-N-factor strategy can be used to determine the transition point. Limiting values for both crossflow and streamwise instability growth are defined by establishing a curve in the $N_{\mathrm{TS}} - N_{\mathrm{CF}}$ plane. Depending on its shape, the interaction between the two transition modes, which cannot be analyzed inside the LST computation, can be captured. Figure 1 shows the curves for the validation cases in this work. The curves feature a moderate interaction by modeling transition below the individual critical N factors with a linear cutaway in the upper-right corner. Essentially, it is assumed that the most unstable TS and CF waves are interacting in the worst possible way and amplify each other such that premature transition occurs at lower individually computed N factors.

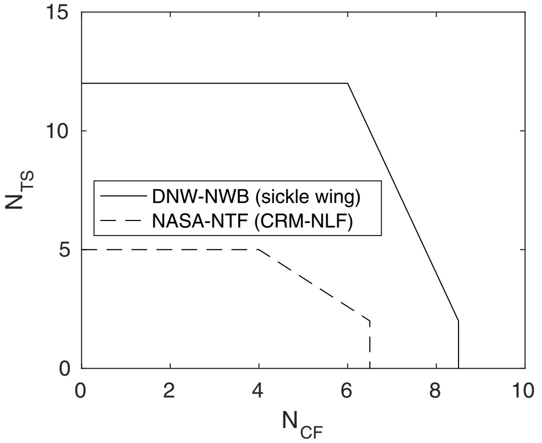

Fig. 1 Critical N factors for the sickle wing and CRM-NLF experiments (transition occurs in the regions above the curves).

IV. RANS–LST Coupling

The goal of this work is to develop an automatic coupling between the flow solver and the LST code. To this end, several steps must be taken. These are outlined in the following sections.

A. Determination of the Maximum Laminar Extent

One problem with carrying out an LST analysis of the laminar boundary layer over a wing is the fact that the Navier–Stokes solver cannot converge to a steady-state solution because of laminar separation when no transition is specified. It is therefore necessary to determine the laminar separation line on the surface that occurs by assuming no previous natural transition. Previously, this has been done using a search algorithm that checks for the most downstream point of transition, yielding a converged RANS solution for two-dimensional geometries. This, however, had two downsides. The first is the purely numerical foundation of the approach, and the second is the immense computational cost when having to look for a separation line on three-dimensional objects. Another possibility is a manual definition of an initial transition line by the user, but this is not ideal in the context of an attempt to automate the tool chain. Krumbein et al. mention that, in their coupling procedure, an initial separation check is performed on the computational RANS grid every 20 to 50 RANS iterations; and the separation location is then directly used as the transition location [7]. For the solver used in this work, however, this was not found to be a robust solution for the implemented coupling because these locations fluctuate highly in the transient RANS solution.

These shortcomings were overcome by performing an iterative procedure between unsteady Navier–Stokes simulations, a shape-factor criterion that determines the onset of laminar separation, and a semiempirical method to determine the separation induced transition length. The laminar separation criterion is based on the energy shape factor $H_{32} = \delta_3/\theta$ that, for laminar boundary layers, has a stagnation value of $H_{32} = 1.620$ and a Blasius flat-plate value of $H_{32} = 1.573$; and it decrease towards separation, occurring exactly at $H_{32} = 1.515$ [31]. A less exact but more robust criterion for the shape factor $H_{12} = \delta^*/\theta$ is added in case $H_{32} = 1.515$ is not reached due to numerical errors. Usually, the shape factor is around $H_{12} = 2.6$ for laminar boundary layers at constant pressure and increases quickly before transition. Because H_{12} increases to approximately 3.5 before laminar separation [32], a limit of $H_{12} = 4.0$ is set for the separation point.

The iterative procedure is started with setting transition at the trailing edge. The unsteady simulation is then run over 2000 time steps with a nondimensional time step of $\Delta t \cdot u_\infty / l_{\mathrm{MAC}} = 0.01$. Subsequently, a separation line is determined with the shape-factor criteria. A semi-empirical estimation method is then used to determine the length between the separation point and the transition point (see Eq. (7) with the longitudinal integral length scale of the flow turbulence $l_s = c/15.8$ as suggested by Roberts [33] and Bernardos et al. [34] for cases where this information is not available):

$$\frac{x_{\mathrm{tr}} - x_{\mathrm{sep}}}{\theta_{\mathrm{sep}}} = \frac{25000}{Re_{\theta_{\mathrm{sep}}}} \log_{10}\left[\coth\left(10\ \max(0.001, Tu_\infty)\left(\frac{c}{l_s}\right)^{(1/5)}\right)\right] \tag{7}$$

The unsteady simulation is then rerun with the updated transition line. An under-relaxation of the transition line movement is applied that reduces the upstream movement of the transition line because overshooting was observed, which then hindered the method from finding the actual separation locations downstream of the first iterations:

$$\tilde{x}_{\mathrm{tr}}^{i+1} = x_{\mathrm{tr}}^{i} + \xi\left(x_{\mathrm{tr}}^{i+1} - x_{\mathrm{tr}}^{i}\right) \tag{8}$$

The relaxation factor is set to $\xi = 0.9$ at the first iteration and is quickly increased toward one in subsequent iterations. Three iterations are usually sufficient to obtain the separation line. Carrying out the unsteady computations was found to be a very reliable way to determine the laminar separation, and the computational costs of these computations are small compared to the overall costs of the simulation of the transition prediction.

In cases where no upstream natural transition occurs, a separation bubble will remain the source for transition and leads to a laminar separation bubble. The sickle wing validation case presented later in the text features this phenomenon. This is illustrated in Fig. 2, where a closeup on the aft part of the inner wing's upper surface is shown. The streamwise velocity component is plotted and reveals the laminar separation followed by a turbulent reattachment of the flow.

B. Converging Laminar–Turbulent Boundary Layer

Once the laminar separation-induced transition line is found, steady computations can be performed. Converging the transitional simulation to a high degree is essential to provide accurate boundary-layer profiles from the base flow to the stability analysis. Here, converged force coefficients are not sufficient because the boundary-layer profiles still change significantly for many more iterations. Instead, the residuals have to be converged sufficiently to ensure fully developed boundary-layer profiles [35,36]. Figure 3 shows a typical convergence history for a RANS simulation on three multigrid levels. Although the force coefficients are already converged after less than half the number of performed iterations, the boundary layers require the 20,000, 7500, and 2500 iterations on the three grid levels to sufficiently converge. These numbers have been found to be a robust choice for the cases considered in this study, and are therefore used throughout this work. Figure 4 shows the convergence of a sample boundary layer on the CRM-NLF wing. The numbers in brackets refer to the iteration count on the finest grid level where the shown line was extracted from the solution. Although the profiles themselves can barely be distinguished from each other, the development of the local relative error with respect to the final solution shows that the flow solution converges.

C. Preparing Boundary-Layer Data for LST

The LST code requires boundary-layer data along a line as input. On a wing, this can be a line over the wing surface in the freestream direction; but, this will not yield good results because, with increasing spanwise flow variations, the instability growth will not follow this direction. Instead, an estimation of the direction of instability growth is applied that is a projection of the boundary-layer edge velocity to the wing surface. Streamlines integrated along these projected velocity vectors are called inviscid streamlines and have been shown to closely resemble the instability group velocity [6,7,23]. They are indicated in the subsequent validation cases (see, e.g., Fig. 5). The LST code requires first and second spatial derivatives of the flow variables with respect to the wall-normal direction. These are determined using the divergence theorem on each finite cell

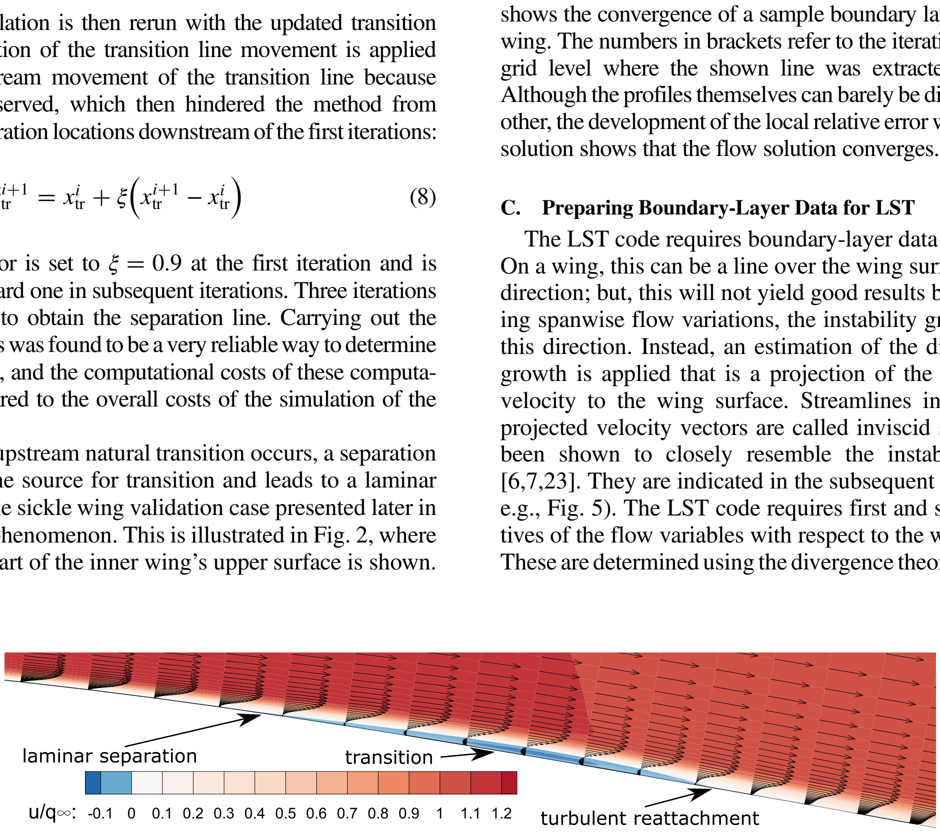

Fig. 2 Streamwise velocity contours and local velocity vectors on the *y* plane at the inner part of the sickle wing (case A) showing a laminar separation bubble.

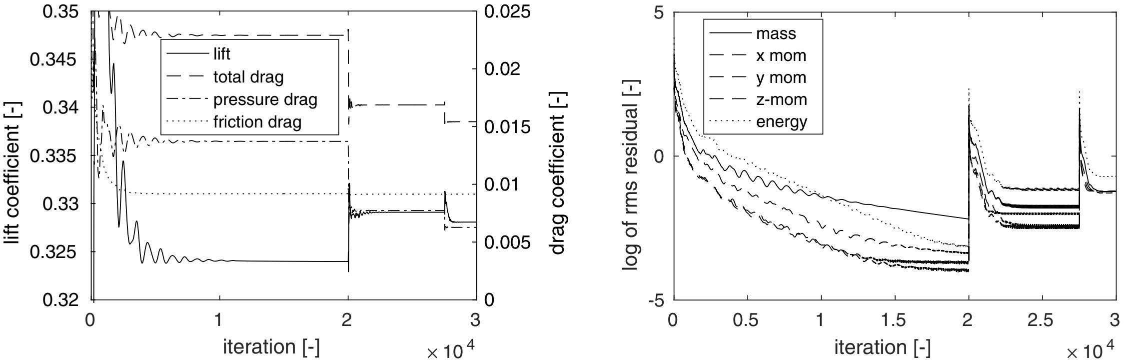

a) Force coefficient convergence **b) Residual convergence**

Fig. 3 Typical convergence history for a CFD run to obtain accurate boundary-layer profiles (jumps caused by multigrid cycles) (mom = momentum).

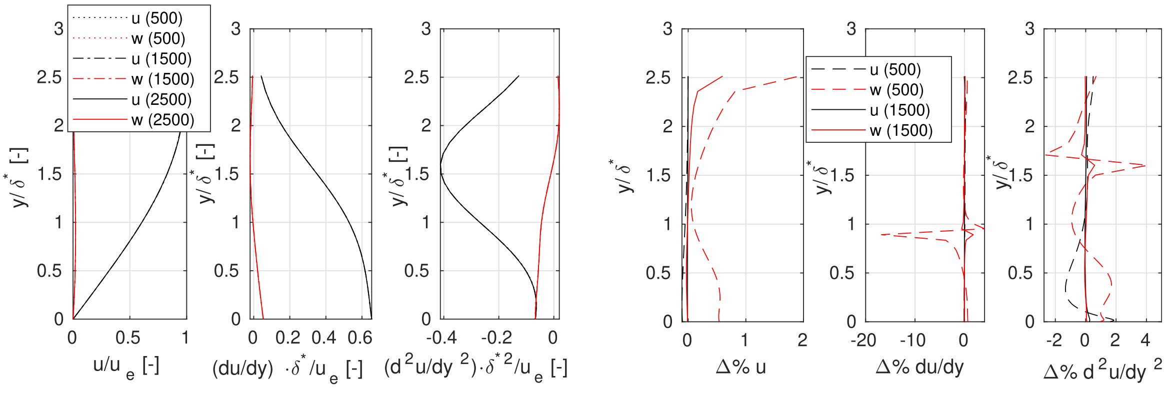

a) Boundary-layer profiles and wall-normal gradients b) Relative errors ($\Delta\% u = (u - u_{2500})/u_{2500} * 100$)

Fig. 4 Convergence of boundary-layer profiles and wall-normal gradients for various RANS iteration counts on the finest grid level (number in brackets).

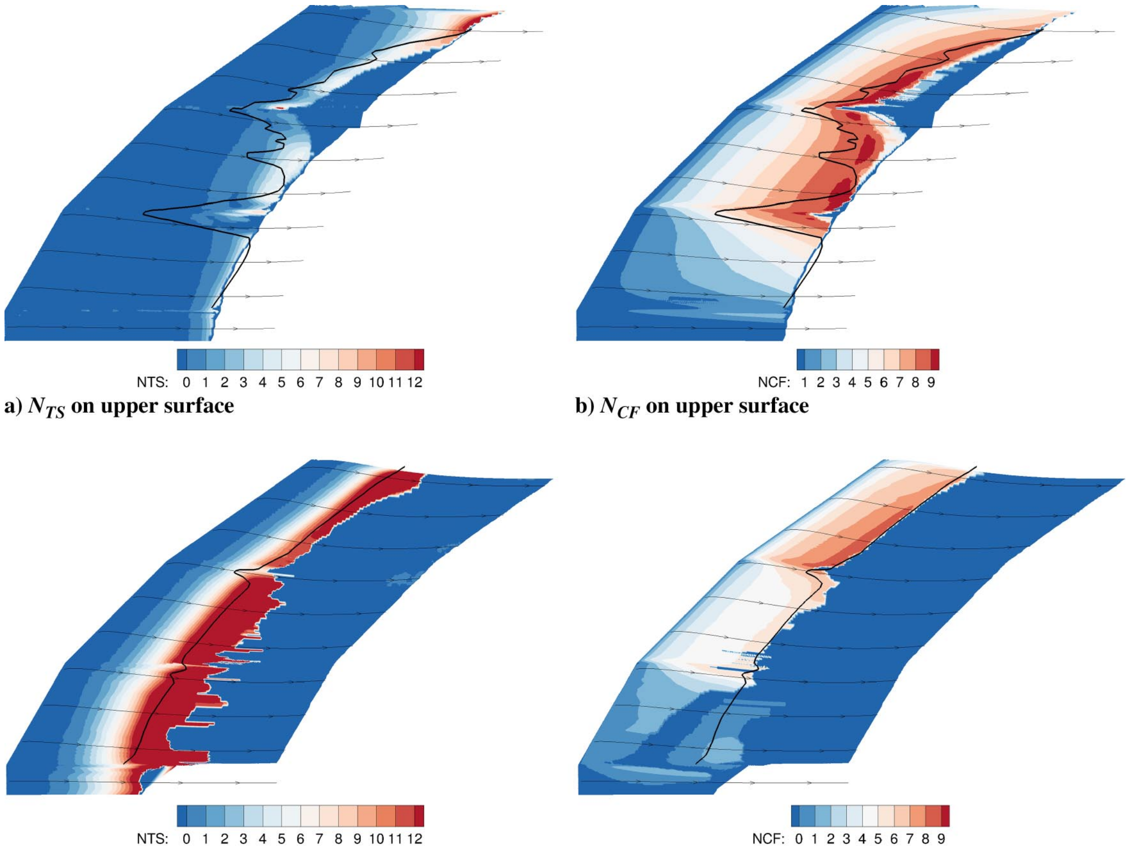

a) N_{TS} on upper surface b) N_{CF} on upper surface

c) N_{TS} on lower surface d) N_{CF} on lower surface

Fig. 5 *N*-factor distributions on sickle wing case A with several indicated inviscid streamlines and the experimental transition lines (solid black lines).

volume in the boundary layer. Subsequently, the flow data are projected onto the LST reference frame.

D. Application of the LST

Depending on the required resolution of the transition line, a certain number of integration lines need to be initiated on the surface in spanwise direction. In the present work, one line per spanwise cell was taken. This may be reduced to save computational effort if little spanwise variation is expected. On each inviscid streamline, the LST analysis is carried out for TS and CF waves. As described in Sec. III, a certain frequency must be specified for assessing a TS wave and a certain wavelength for a CF wave.

The most unstable modes, however, are unknown; as such, a sweep is required in a range of physically meaningful frequencies and wavelengths. For the TS instabilities, a frequency sweep is performed while the CF instabilities are assessed with a wavelength sweep. This process can be fully parallelized since the computations for varying frequencies/wavelengths and on different integration lines are completely independent of each other.

E. Using the Two N-Factor Strategy to Find the Transition Line

The resulting N-factor curves from the aforementioned linear stability analysis are translated into transition lines by means of a two-N-factor approach. A streamline starts at $N_{\mathrm{TS}} = N_{\mathrm{CF}} = 0$ and then features increasing growth factors when encountering unstable regions. A critical $N_{\mathrm{TS}} - N_{\mathrm{CF}}$ curve is defined, and transition is assumed where the computed N factor exceeds the critical N factors. An example can be seen in Fig. 1 for the validation cases used in this work. This includes tests in NASA's National Transonic Facility (NTF) and the German-Dutch Wind Tunnels' (DNW) low speed windtunnel (NWB). These lines are different, depending on the freestream flow quality [as follows from Eq. (6)]. The critical N factor is affected not only by the freestream turbulence but also by other disturbance-generating influences like the sound pressure level in the wind tunnel or surface roughness on the wing model. Furthermore, various other flow characteristics like the Reynolds number, compressibility, and the injection of liquid nitrogen possibly all have an influence on the N factors [21,23,37]. Notably, under the used test conditions, the curve for NASA's National Transonic Facility has a higher freestream turbulence than the low-speed wind tunnel of the German–Dutch wind tunnels, leading to lower critical N factors. In both cases, some interaction between streamwise and crossflow instabilities is observed, leading to premature transition below the individual critical N factors.

To obtain the critical N-factor curve for a certain flow, linear stability analyses must be performed on an experimentally or computationally obtained mean flow to identify the growth factors at which transition is observed. This means that initial experimental effort is necessary for each environment (e.g., a certain wind tunnel or free flight) to calibrate the methodology before it can be used on other geometries, angles of attack, or other variations that do not significantly change the critical N factors. It can be seen from the results in Sec. V, however, that a single limiting N-factor curve is able to predict transition from LST results reasonably well across an entire configuration and varying Reynolds numbers as well as angles of attack.

Because of the direct coupling between the flow solver and the linear stability analysis, the instability of the separated laminar flow can also be analyzed. It should be noted, however, that the parallel flow assumption is violated in the case of separated flow. The main focus of this work, however, is not to resolve laminar separation bubbles but to identify the locations of natural transition of mostly attached flows.

F. Applying New Transition Line and Iterate

Once the new transition lines are determined, they can be applied to the next RANS simulation. The change in boundary-layer flow again has an effect on the LST analysis, and so several iterations have to be performed. Usually, three to four iterations were found sufficient for convergence, meaning a negligible movement of the transition line in the order $|\Delta x_{\mathrm{tr}}| = |x_{\mathrm{tr}}^{i} - x_{\mathrm{tr}}^{i-1}| \approx 0.1\% c$, which is in line with the numbers provided by Krumbein et al. [7]. Because overshooting was observed during the upstream movement of the transition line, an under-relaxation factor ζ is applied. A value of $\zeta = 0.75$ was found to be a robust choice for three-dimensional problems:

$$x_{\mathrm{tr}}^{i} = x_{\mathrm{tr}}^{i-1} + \zeta\left(x_{\mathrm{tr}}^{\mathrm{LST}} - x_{\mathrm{tr}}^{i-1}\right) \tag{9}$$

Figure 6 shows a schematic of the full coupling and the iteration procedure (similar to Ref. [7]).

G. Convergence Study

Due to the sensitivity of the transition prediction to accurate boundary-layer input data and the resulting requirement for fine grids, a convergence study has been performed to identify the influence of grid refinement and simulation convergence on the predicted transition lines.

The density of the finest grid level is varied to find the required number of wall-normal cells. Three different grid densities have been used: a coarse grid with 30–35 cells, a medium grid with 60–70 cells, and a fine grid with 120–140 cells in the boundary layer. The boundary-layer thickness is determined in the flow solver using an algorithm based on a Baldwin–Lomax function [38] from which the number of cells in the wall-normal direction are found.

Figure 7 shows that, in the current study, a number of 60–70 cells is sufficient to accurately predict the profiles. This coincides precisely with the numbers mentioned by Stock and Haase in their work [39]. It was furthermore reported by Krumbein et al. [5] that a number of approximately 130 cells within the prismatic grid layer would be required to obtain sufficiently accurate boundary-layer profile derivatives to assess crossflow transition. With the growth in transitional and turbulent boundary layers downstream of the transition line, similar numbers are found in this study for the total number of grid points in the near-body grid containing the viscous layer. Although the velocity profiles and their first spatial derivative with respect to the wall-normal direction are very similar between the different grid densities, a significant difference can be seen for the second derivative on the coarse mesh. The maximum difference and the L2-norm difference of the second derivative were found to have a second-order convergence rate. The maximum relative difference is approximately 40% between the coarse and the medium grids and roughly 10% between the medium and the fine grids. For the L2 norm, the numbers are 10 and 2%, respectively.

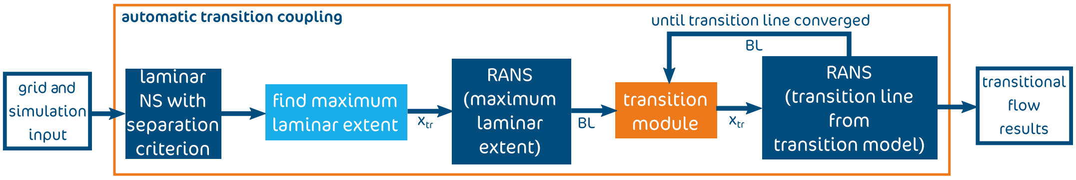

Fig. 6 Schematic of the coupling procedure.

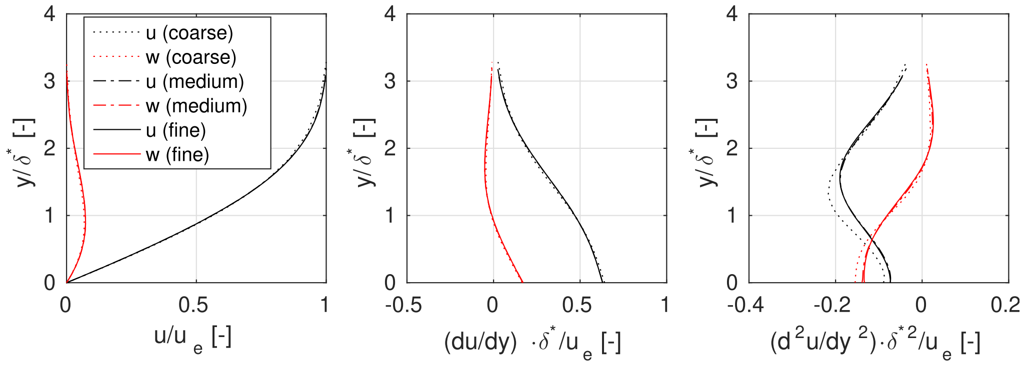

Fig. 7 Mesh convergence for exemplary streamwise and crossflow boundary-layer profiles as well as wall-normal derivatives on quarter-chord of sickle wing case A.

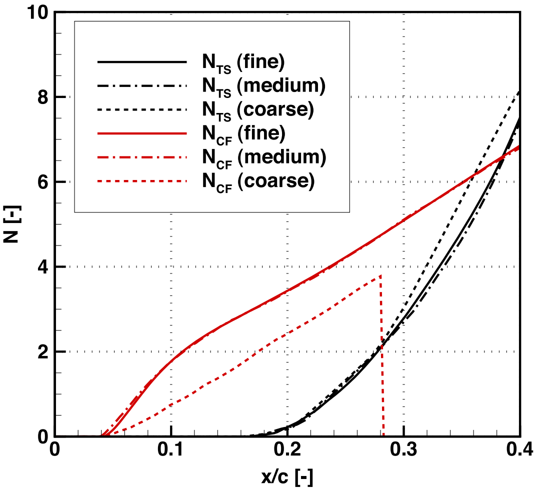

Fig. 8 Mesh convergence for exemplary *N* curves on sickle wing case A.

To also show that the resulting amplification rates obtained from the linear stability analysis are sufficiently accurate with the medium grid, two examples for each streamwise and crossflow *N* curve are shown in Fig. 8, which are obtained from sickle wing case A (see Sec. V.A). It is indeed the case that, although the coarse mesh does capture the growth trend, it is not accurate enough to predict a transition location and even fails to find amplification factors in clearly unstable regions. The medium and fine grids result in nearly identical amplification rates. To obtain a low required number of cells, the accuracy of the flow solver is important. In this study, the structured flow solver simulates the boundary layer using a matrix dissipation scheme with a very low amount of artificial dissipation. Care was taken to preserve accuracy throughout the coupling procedure, e.g., by using a finite volume scheme to determine the boundary-layer profile derivatives and a subsequent linear interpolation to the inviscid streamline coordinates.

Lastly, the required number of iterations for the coupling was assessed. As shown in Fig. 9, the transition line can still change over several percent of the chord length after the first iteration; but afterward, it barely moves any more. Generally, convergence (movement of less than $1\% x/c$) occurs after three to four iterations in the present cases.

V. Application of the Automatic Transition Prediction Method

Two validation cases were selected to assess the ability of the methodology to predict transition on wall-bounded flows with high Reynolds numbers and low freestream turbulence levels, namely, the TU Braunschweig sickle wing experiment [40] as well as the CRM-NLF geometry designed at NASA Langley Research Center [41].

Table 1 Conditions for sickle wing test cases

Case	Re_c	M	α, deg
A	$2.744 \cdot 10^6$	0.156	−2.6
B	$4.448 \cdot 10^6$	0.259	−2.6
C	$4.434 \cdot 10^6$	0.259	−0.3
D	$2.748 \cdot 10^6$	0.158	6.0

A. Sickle Wing Experiment

The sickle wing was specifically designed at TU Braunschweig to serve as a benchmark test case for transition prediction tools [40]. As such, it was given a planform that features differing sweep angles (30, 45, and 55 deg) and a small blending radius (5 mm) between the individual segments. The result is that for a single flow condition, various (interacting) transition mechanisms occur at different positions on the wing. The wing was tested in the DNW low-speed wind tunnel in Brunswick, Germany at a turbulence intensity of $Tu = 0.053\%$ at $u_\infty = 60\ \mathrm{m/s}$.

Two different Reynolds numbers ($2.7 \cdot 10^6$ and $4.4 \cdot 10^6$) and two different angles of attack (−2.6 and −0.3) are compared to the numerical results from Kruse et al. [42] in the following. The conditions for the tests are summarized in Table 1. The fourth test condition (case D) at an elevated angle of attack is not taken into account in this study because the wind-tunnel walls are not modeled in the simulations and wind-tunnel effects are assumed to significantly change the results at higher angles of attack for a wing that is relatively large compared to the test section size.

The low turbulence in the test section results in relatively large limiting *N* factors for transition, as shown in the two-*N*-factor curve in Fig. 1. The curve was obtained by comparing the experimental transition line and the *N*-factor distributions obtained from COSALX, initially using the growth factor limits ($N_{\mathrm{TS}} = 11.8$ and $N_{\mathrm{CF}} = 8.4$) provided by Kruse et al. [43] and slightly increasing the limiting TS growth factor to better match the transition lines for all three cases. Additionally, a cutoff was added to account for moderate interactions between simultaneously existing TS and CF modes as already indicated by Kruse et al. Comparing the calibrated curve to the values reported by Kruse et al., it can be noticed that similar values are found at $N_{\mathrm{TS}} = 12.0$ and $N_{\mathrm{CF}} = 8.4$ in this work.

The wing is discretized using an O-type grid with wall-normal expansion in the relevant areas for transition prediction. The surface is divided into 336 spanwise cells and 240 chordwise cells for each upper and lower surface (see Fig. 10). With an average of $y^+ = 0.1$, the first off-wall cell height is small enough to resolve the viscous sublayer. One-hundred and ten to 140 cells are within the boundary layer to provide accurate profiles to the stability analysis. The convergence study has shown that less points are sufficient, which is beneficial for future investigations, including the second validation case in Sec. V.B. The total number of grid cells is $42 \cdot 10^6$. The computational domain expands to 40 chord lengths in all directions,

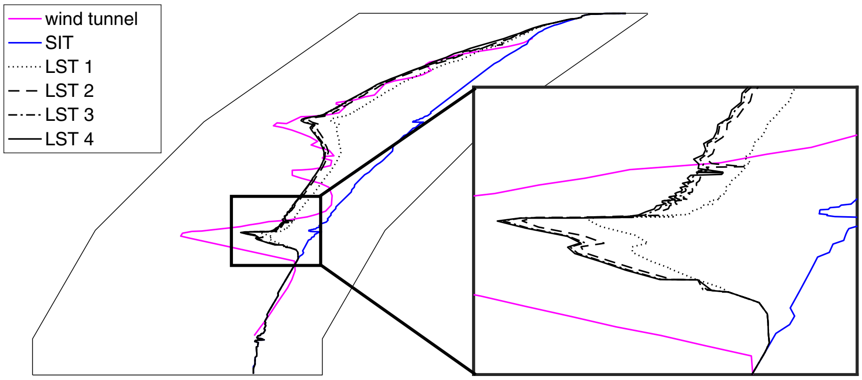

Fig. 9 Movement of transition line during LST iterations 1 to 4 with under-relaxation ($\zeta = 0.75$) on sickle wing case A.

except for the downstream direction where 60 chord lengths are selected.

This case shows very fast convergence of the transition line as shown in Fig. 9. Already, the second iteration has only small variations with respect to the first iteration. The second and third iterations can no longer be distinguished visually anymore.

Figure 11 shows a comparison of the experimental and the numerical pressure distributions at the centers of the three sections. Case A is left out because it is nearly identical to case B. The CFD results closely resemble the measurements. As such, a good mean flow should be obtained for the LST analysis. Also, the resolved laminar separation bubble can be visually seen for the upper-surface inboard section (30 deg sweep angle) for case C at approximately 75–80%x/c.

For case A, the resulting N-factor contours on the wing surface are shown in Fig. 5 for TS and CF instabilities. Although, in reality of course, LST computations are performed on individual inviscid streamlines (some are included in the image) and not globally on the entire wing surface; visualizing the N-factor growth in this way gives a better understanding of how transition occurs over the span of the wing. The contours are obtained by triangulation of the individual streamlines that run from the leading edge until the separation-induced transition line because the LST computation is only run until this point to save computational costs. The experimental transition lines are included to show which mechanism triggers transition.

On the upper surface, a negative pressure gradient exists up to approximately three-quarters of the chord, where laminar separation would occur in case of no prior transition. As such, only the very rear of the upper surface shows TS wave amplification. The same holds for the lower surface: only the suction peak is already reached at roughly 20% of the chord.

The crossflow wave amplification is clearly increased in the kink regions on both surfaces. This is not unexpected because strong variations in crossflow exist in this region due to the quick geometric changes. Additionally, the lower surface nicely shows how, despite the similar pressure distribution in the leading-edge region of all three sweep angles, an increase in N_{CF} is obtained by increasing the sweep angle. As a higher sweep angle increases the spanwise pressure differences, higher crossflow also occurs even if a constant profile with similar streamwise pressure distribution is used.

On the upper surface, larger variations in the pressure distribution exist in the half-chord region. As such, larger variations in N_{CF} are also observed. Especially the effect of the tip can be noticed, which apparently leads to reduced CF instability. As such, transition on the upper surface is dominated by CF transition, except for the tip where TS instabilities are amplified significantly. This is consistent with the experimental line showing a transition line with wedges, which is typical for crossflow transition. On the lower surface, TS transition dominates in the inner section but mixed transition occurs with stronger CF instabilities toward the tip. Nevertheless, TS waves are dominating, and this is indicated by the very straight experimental transition line.

Figure 12 shows the N-factor contours for case B at an elevated Reynolds number. The upper side remains dominated by crossflow transition. A general increase in crossflow N factors can be observed

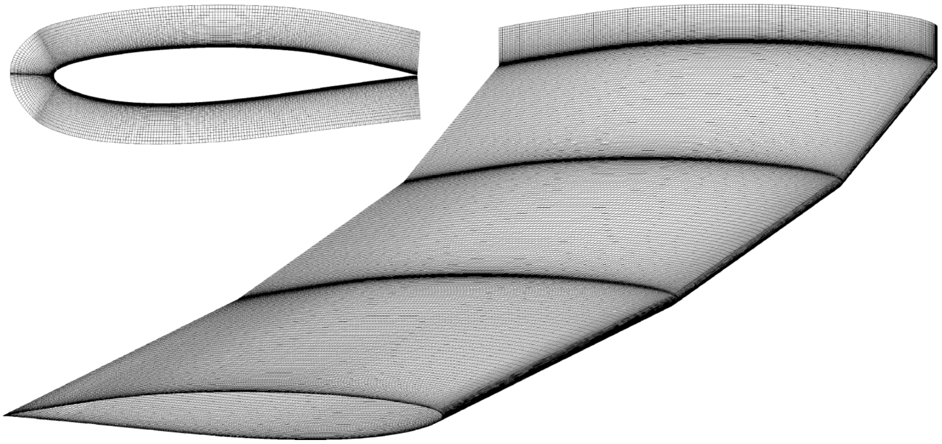

Fig. 10 Surface and wall-normal mesh on sickle wing (SIT = separation induced transition).

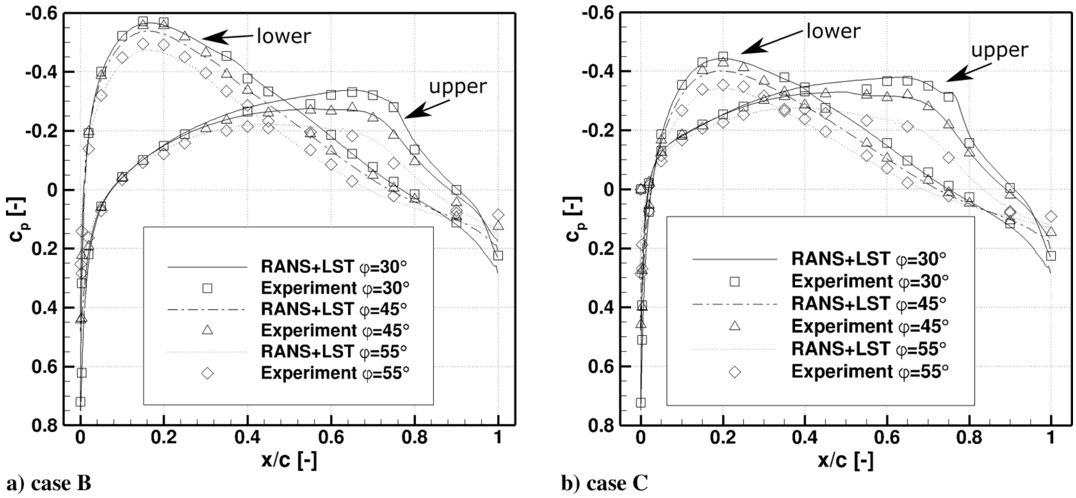

a) case B

b) case C

Fig. 11 Pressure distributions on sickle wing upper and lower surfaces at the centers of the three sweep angle sections.

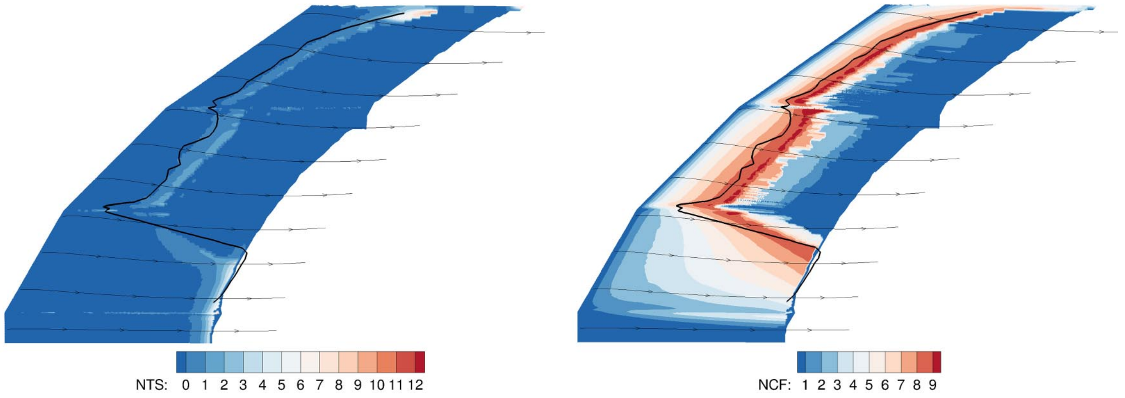

a) N_{TS} on upper surface **b) N_{CF} on upper surface**

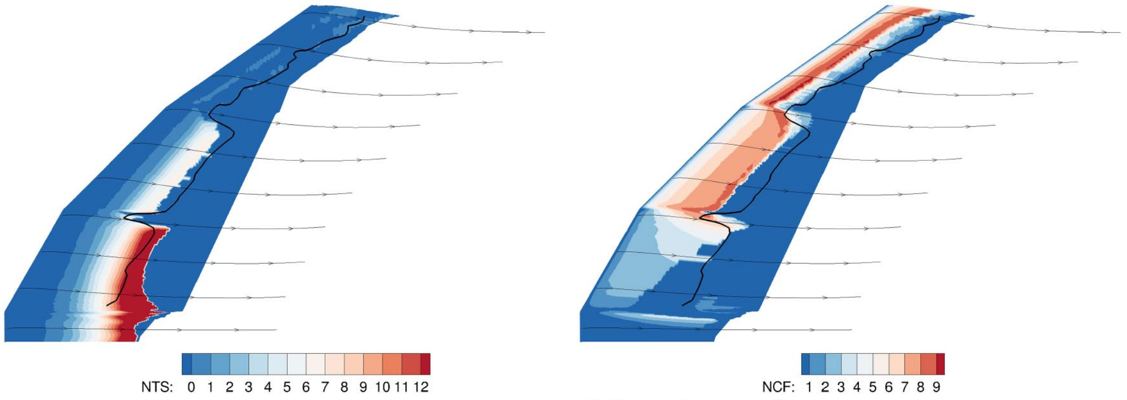

c) N_{TS} on lower surface **d) N_{CF} on lower surface**

Fig. 12 ***N*-factor distributions on sickle wing case B with several indicated inviscid streamlines and the experimental transition lines (solid black lines).**

as expected for the increased Reynolds number. On the lower side, mixed transition still dominates the midsection, crossflow instabilities cause transition in the outer section, and streamwise instabilities dominate the inner section.

The N contours for case C (see Fig. 13) show how the higher angle of attack leads to less crossflow instability growth on the upper surface. The pressure distributions feature a steeper slope toward the end of the strong pressure drop up to $x/c \approx 0.05$ and then stay flatter within the range $0.05 \lesssim x/c \lesssim 0.2$ compared to the previous case. This reduces the amount of crossflow, and thereby delays transition. On the lower side, however, crossflow waves are more amplified very close to the leading edge. This is caused by the more gradual drop in pressure in the chordwise direction in this region. When combined with a sweep angle, this leads to higher spanwise pressure gradients, and thus more crossflow. The streamwise instabilities are barely affected by the increase in α.

The separation-induced transition at the upper inner section of the wing shows that the shape-factor criterion together with the transition length correlation lead to a slightly earlier transition than expected from LST as the N factors reach the limiting values slightly behind the predicted location. Figure 9 shows for case A that at the inboard section, no transition is found from the LST upstream of the separation-induced transition front. Instead, transition is enforced at the estimated separation-induced transition length downstream of the separation location. The section cut in Fig. 2 shows that a small separation bubble over nearly 5% of the chord length at $x/c \approx 0.75$ forms. A clearly recognizable bubble is, however, only observable up until approximately 16% of the span for both cases A and B. The remainder of the inboard section shows no sign of a separation bubble, suggesting nearly instantaneous transition at the separation location. It should further be noticed that the first 10% of the span is influenced by a turbulent boundary layer of the wind-tunnel wall in the experiments. Only in case C does the stability analysis predict transition upstream of the separation-induced transition front across the entire span, and no separation is found.

The resulting skin-friction coefficients for cases A, B, and C are shown in Fig. 14; and the experimental transition lines are again included for comparison. In general, the experimental and numerical results compare well, but some differences can be observed. Laminar separation is accurately captured in all three cases. All cases feature laminar separation and the resulting separation-induced transition at the upper inner section.

Case A shows very good agreement on the lower surface where even the small wiggles in the kink regions are resolved with the stability analysis. On the upper side, a difference can be seen around the inner kink where the strong geometrical changes and the resulting spanwise pressure gradients seem to cause a locally nonparallel flow violating the assumptions made in the stability analysis. Also, in the center segment, strong variations in the transition location are not obtained using LST. The experimental results are believed to be affected by the pressure tabs in the location of sudden upstream movement of the transition line, leading to a turbulent wedge downstream. Similar differences were also observed in other studies using the same validation case (see, e.g., the work of Kruse et al. [42]).

Case B is generally well predicted across the entire surface. The "wiggly" experimental line on the lower side already indicates the stronger influence of crossflow transition on the flow at this elevated Reynolds number, especially in the mid- and outboard segments. These areas also show the biggest difference in the experimental lines. Although the trend is followed nicely, the transition line is predicted upstream a few percent of the chord length compared to the experiment.

Case C shows good agreement as well. The only big difference is the underestimation in the crossflow wedge at the inner kink on the upper surface, as already observed in case A. The experimental transition line on the lower side is well reproduced by the simulation

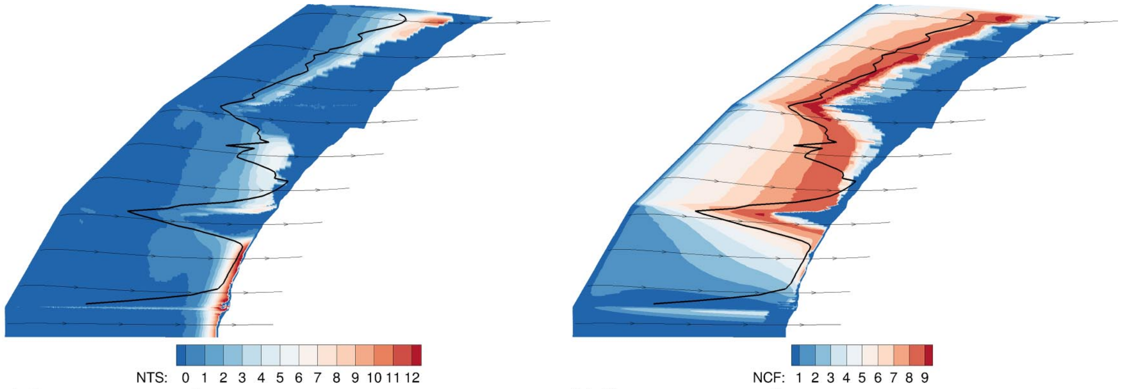

a) N_{TS} on upper surface

b) N_{CF} on upper surface

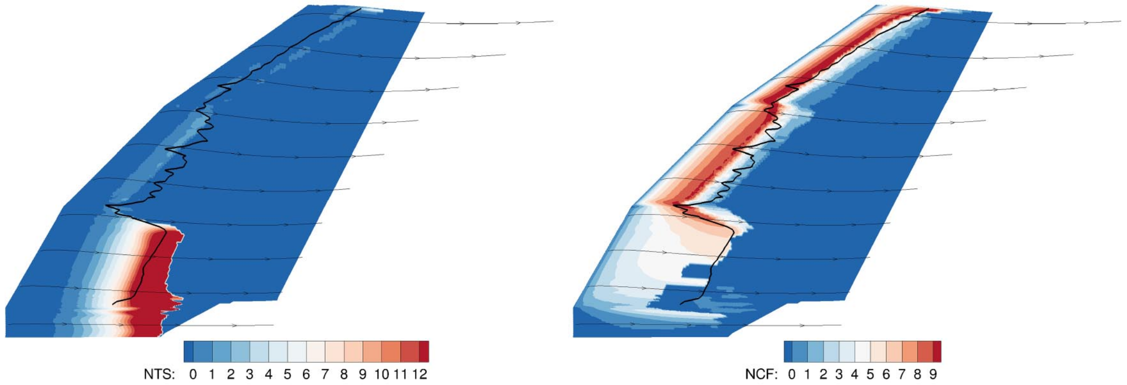

c) N_{TS} on lower surface

d) N_{CF} on lower surface

Fig. 13 ***N*-factor distributions on sickle wing case C with several indicated inviscid streamlines and the experimental transition lines (solid black lines).**

and only shows a slightly early prediction in the outboard regions. A possible explanation of the early prediction of transition for the lower side outboard sections on cases B and C could be the high streamline curvatures in these areas: an effect that has been neglected in the LST computations.

B. Common Research Model: Natural Laminar Flow Wing

The NASA Common Research Model (CRM) wind-tunnel experiments have successfully served as benchmark CFD cases in many studies. NASA's newly designed natural laminar flow CRM wing [41] for the aircraft was tested in the National Transonic Facility using temperature-sensitive paint [44]. The transition location was made visible by heating the surface of the wing model using a carbon-based heating layer. At a high Reynolds number of $Re = 15 \cdot 10^6$, a Mach number of $M = 0.86$, and a turbulence intensity of $Tu \approx 0.24\%$, and various angles of attach (see Table 2), this case allows for an assessment of the capability of the transition prediction methodology to simulate aircraft wings under typical cruise conditions. The compressibility of the flow is an especially big difference compared to the low subsonic regime of the sickle wing.

Lynde et al. report that after their wind-tunnel corrections for the experimental data, no corrections were required for the CFD computations [45]. Mach and alpha shifts were applied to the CFD computations in this work to better match the pressure distributions of the wind-tunnel experiment. Variations in Mach number are mainly attributed to systematic wind-tunnel errors, and are therefore equal for all cases. The change in angle of attack, on the other hand, is probably caused by wing deflections and is not constant under varying wing loading, whereas one deflected shape (based on the design lift coefficient $C_L = 0.5$) is used for the computational mesh for all conditions. The Mach numbers of the CFD computations were shifted by $\Delta M = M_{\mathrm{CFD}} - M_{\mathrm{WT}} = -0.003$, and the angle of attack was varied by $\Delta\alpha = \alpha_{\mathrm{CFD}} - \alpha_{\mathrm{WT}}$ with changing values in the range of $-0.05\ \mathrm{deg} \leq \Delta\alpha \leq -0.2\ \mathrm{deg}$.

The mesh is structured as an O-type grid around the wing and as a C-type grid around the fuselage with a symmetry plane at the centerline of the fuselage. The wing surface mesh (see Fig. 15) has 348 spanwise cells and 240 cells in the chordwise direction on each upper and lower surface. The near-body grid is oriented normal to the surfaces with an averaged first cell height of $y^+ = 0.3$. Depending on the local boundary-layer thickness, the number of points in the boundary layer varies between roughly 30 and 140 cells. At the locations of interest for the stability analysis (i.e., shortly downstream of the leading edge up to the transition front), 60 to 80 wall-normal cells are within the boundary layer. This is inline with the required grid density found from the convergence study of the sickle wing. The total mesh around the half-model has $106 \cdot 10^6$ cells in 2830 blocks. The domain extends by 100 semispan lengths in all directions.

Transition was only analyzed for the suction side of the wing. The pressure side was tripped in the experiment at 5% of the chord length by trip dots applied in five straight lines (i.e., locally, not exactly, 5% in the curved inboard section). On the fuselage, the boundary layer was tripped at 1.5% of the fuselage length downstream of the nose. The resulting intermittency on these surfaces is shown in Fig. 16. The two-N-factor curve found from the LST analysis with critical N factors of $N_{\mathrm{TS}} = 5.0$ and $N_{\mathrm{CF}} = 6.5$ is within the range of the critical N factors of $4.0 \leq N_{\mathrm{TS/CF}} \leq 7.0$ as reported by Lynde et al. [44]. For the calibration, it was initially started with the center of the mentioned range for both N factors. It was noticed, however, that the crossflow N factor reaches values near six near the leading edge for case 1 without observing transition in this region. It was therefore increased to 6.5. The Tollmien–Schlichting N factor was slightly lowered to $N_{\mathrm{TS}} = 5.0$ because late transition was observed at TS-dominated transition locations with $N_{\mathrm{TS}} = 5.5$. From the LST results, it was furthermore clear that mixed transition leads to premature transition at several locations. To resolve this with the two-N-factor curve, a cutoff was added.

Figure 17 shows the pressure distribution at the locations where pressure measurements were taken on the wing over the full chord. The CFD results match the wind-tunnel measurements reasonably

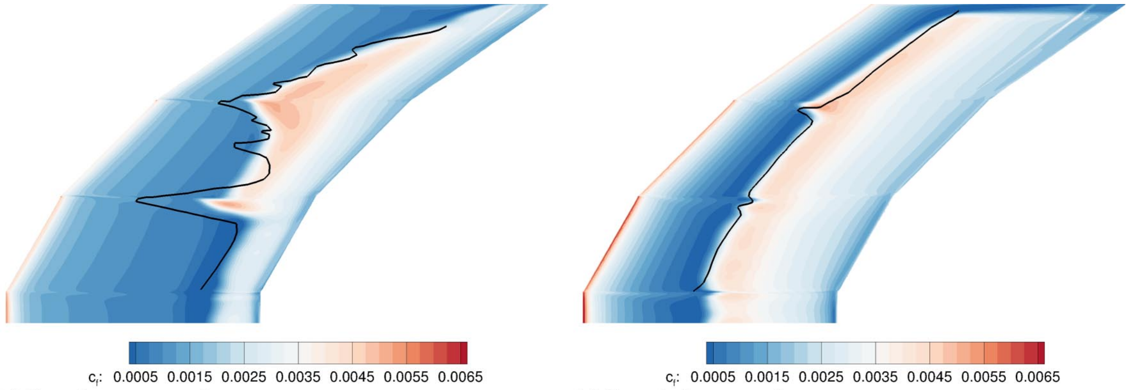

a) Case A: upper surface

b) Case A: lower surface

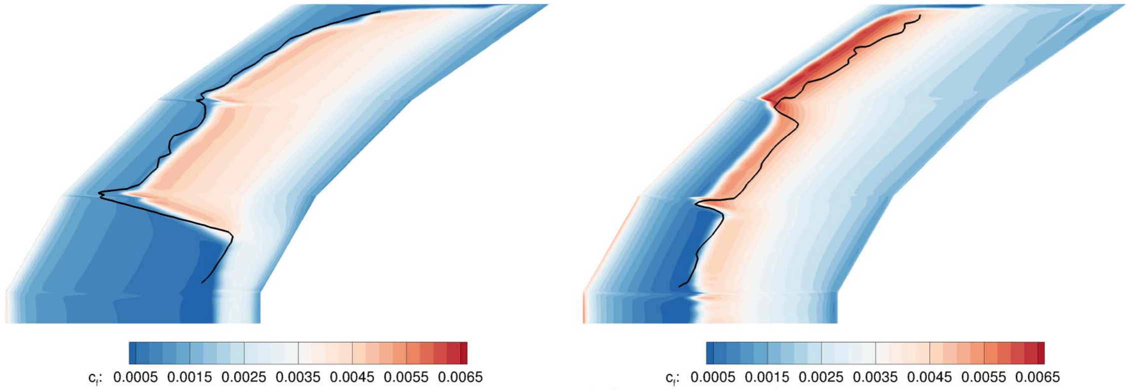

c) Case B: upper surface

d) Case B: lower surface

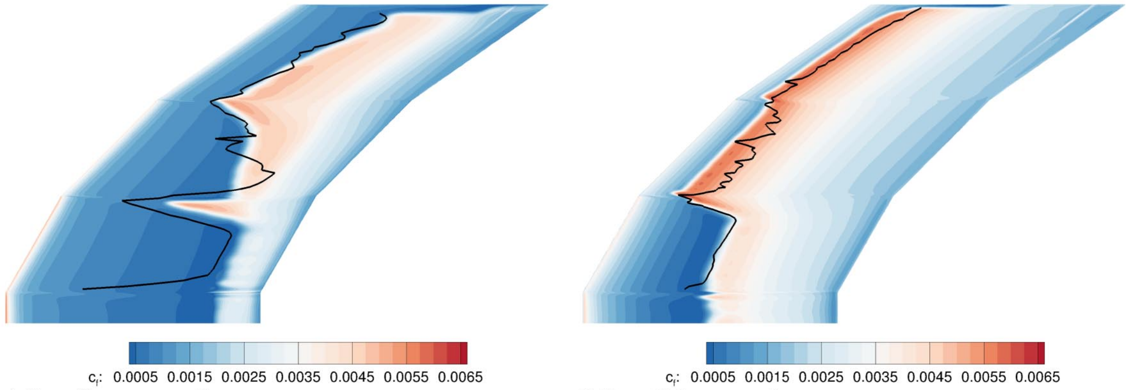

e) Case C: upper surface

f) Case C: lower surface

Fig. 14 Skin-friction coefficient contour on sickle wing cases A, B, and C resulting from RANS–LST coupling and indicated transition lines from experiment (solid black lines).

well. For the lower two load cases, the suction at $0.0 \leq x/c \leq 0.2$ is slightly underestimated. This difference can be attributed to the nonperfect twist and bending of the available CAD model, and hence the computational grid being the same for all four load cases. Another notable difference is the slight overprediction of the pressure plateau at the two inboard sections within the range $x/c \gtrapprox 0.3$ and the shock location on the upper surface for all cases. Finally, the subtle suction peak at the inboard location on case 4 shows a somewhat quicker drop in the computations. Nevertheless, shock locations and pressure variations are reasonably well predicted, which is considered suitable for the stability analysis to predict transition locations accurately.

Table 2 Conditions for CRM-NLF test cases

Case	Re_{MAC}	M	α, deg
1	$14.97 \cdot 10^6$	0.8565	1.45
2	$14.95 \cdot 10^6$	0.8565	1.98
3	$14.91 \cdot 10^6$	0.8561	2.46
4	$14.85 \cdot 10^6$	0.8558	2.94

Figures 18 and 19 show the N factors found from the stability analysis. Both contours for streamwise and crossflow instabilities are shown and reveal a complete change in the mechanisms responsible for transition between the lower and higher angles of attack. Again, the LST code was run from the leading edge to the laminar separation line only to avoid unnecessary use of resources.

At design conditions (case 4), only minor crossflow modes are found to be unstable at the leading edge. At the remaining wing, no crossflow instabilities are found. The reason can be found in Fig. 17,

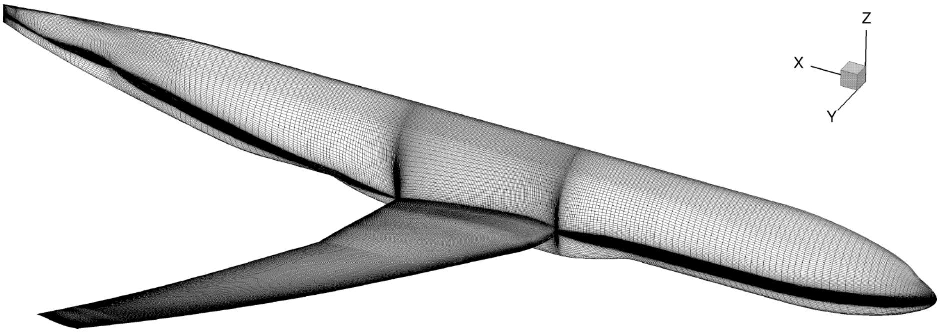

Fig. 15 Surface mesh on CRM-NLF.

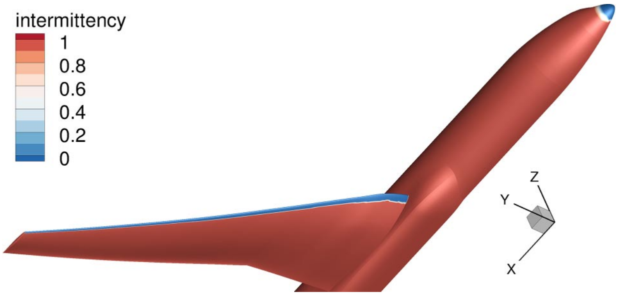

Fig. 16 Boundary-layer tripping on CRM-NLF.

which shows a rapid drop in pressure at the leading edge, followed by a nearly flat pressure plateaus across the span until the shock location. This design methodology as described by Lynde and Campbell [41] suppresses the occurrence of strong spanwise crossflow variations and dampens the instabilities. The plateau is furthermore making the boundary layer just stable enough to prevent streamwise instabilities to cause transition. Because of this, transition occurs only at the onset of the shock where streamwise instabilities get significantly amplified in the outboard wing at $2y/b \geq 67\%$. Inboard of the kink, however, a positive pressure gradient can be observed in the leading-edge area that results in transition at roughly 10% of the chord.

Case 3 leads to very similar growth factors, apart from the onset of crossflow instability growth in the outboard half of the wing. The increase in spanwise pressure variation and the resulting growth in crossflow have a direct effect on the growth of crossflow instabilities. The amplification is, however, not yet strong enough to cause transition.

At reduced angles of attack (cases 2 and 3), the pressure distributions mostly show reduced positive pressure gradients near the leading edge and, for case 2, even feature moderate negative pressure gradients upstream of the shock location. Hence, the streamwise instabilities are significantly reduced. Furthermore, the less uniform pressure plateaus for cases 2 and 3 and the curved chordwise pressure distributions for case 3, paired with the sweep angle, lead to strong spanwise pressure

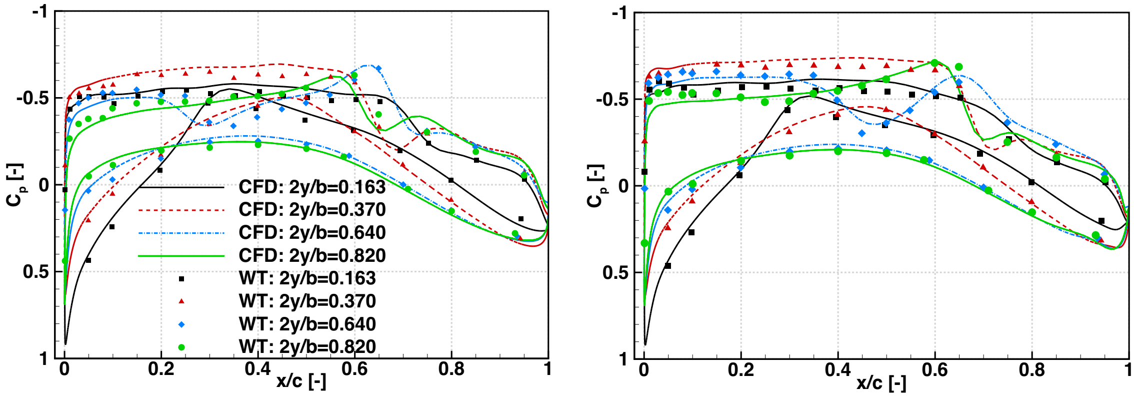

a) Case 1

b) Case 2

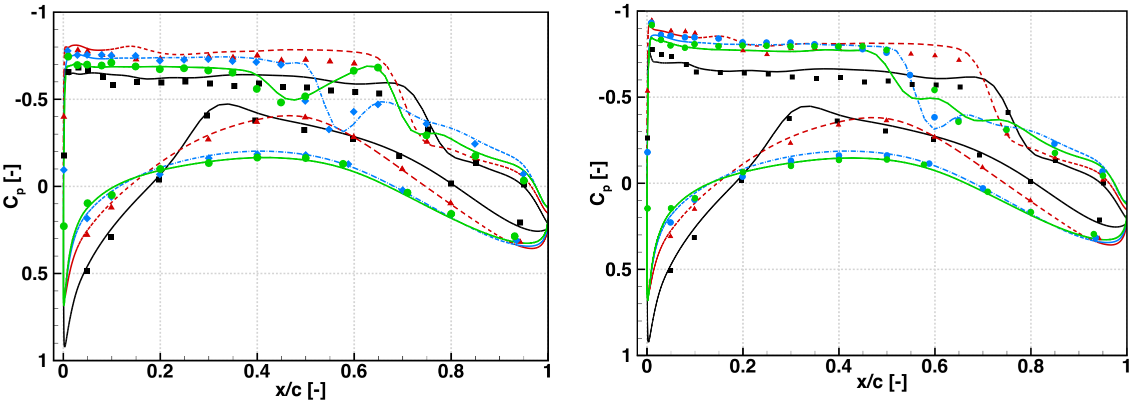

c) Case 3

d) Case 4

Fig. 17 Pressure distributions on CRM-NLR for cases 1 to 4 (WT = wind tunnel).

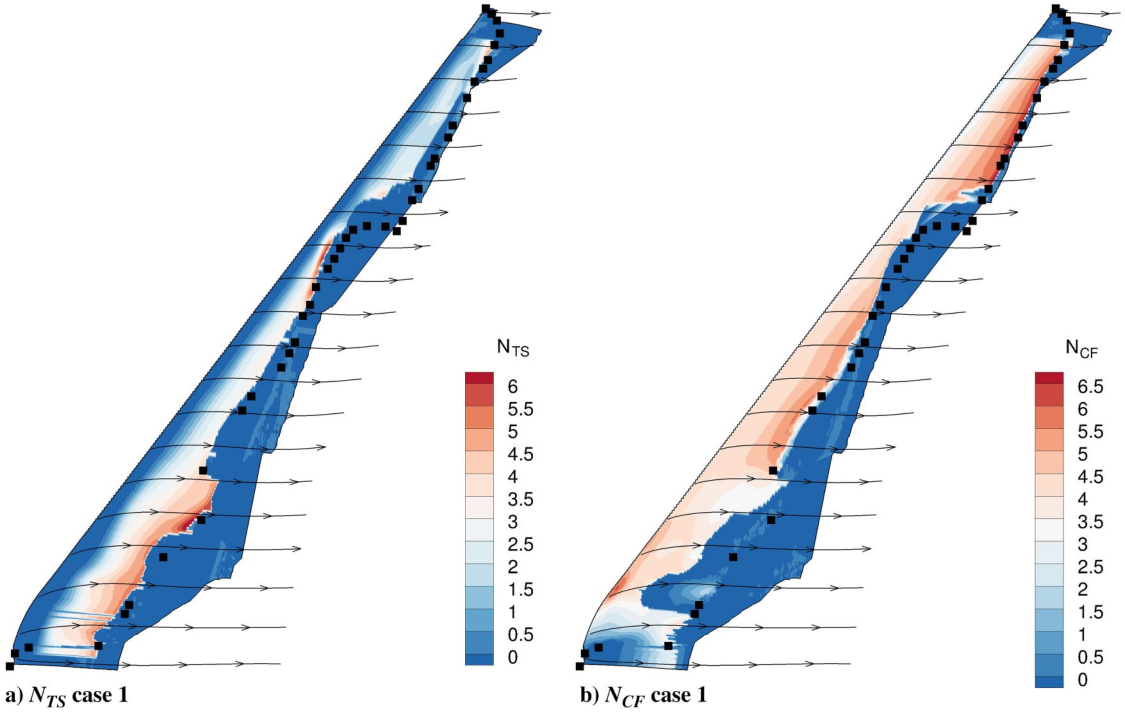

a) N_{TS} **case 1** **b)** N_{CF} **case 1**

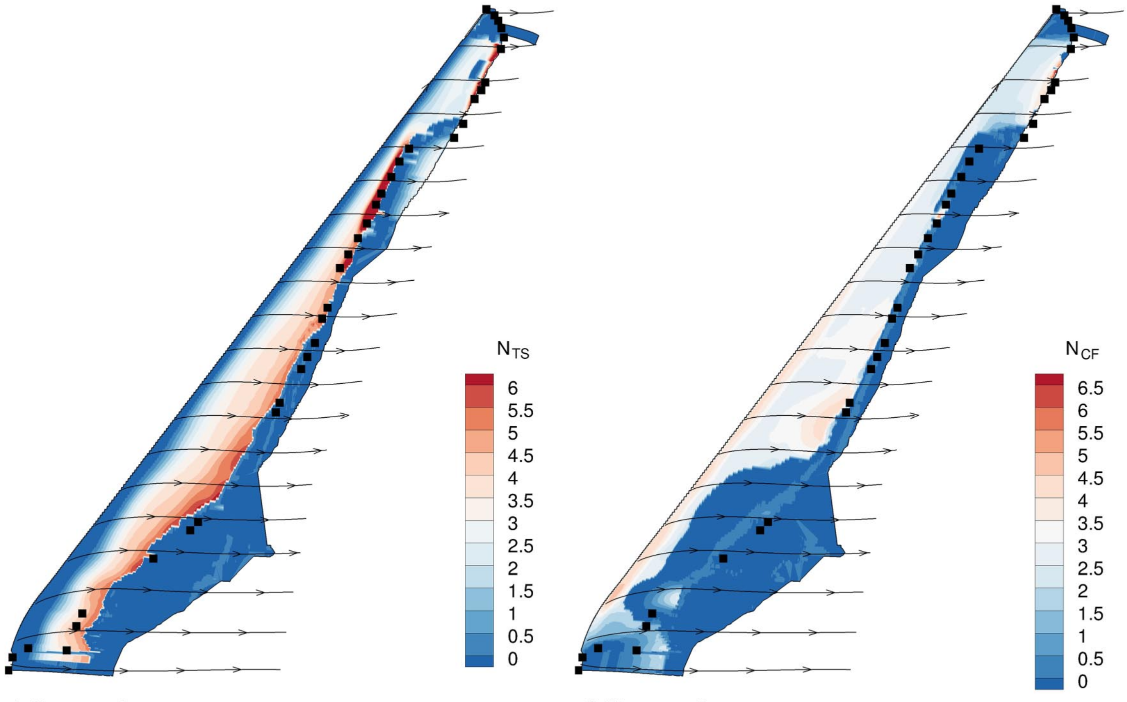

c) N_{TS} **case 2** **d)** N_{CF} **case 2**

Fig. 18 ***N*-factor distributions on CRM-NLF with several indicated inviscid streamlines (cases 1 and 2) and transition points from experiment (black squares).**

variations, and hence increase the crossflow components of the flow. This can be observed for the leading-edge area where the transition to the pressure plateau until $x/c \approx 5\%$ is much more gradual compared to the higher angles of attack, as well as in the downstream region upstream of the shock where the chordwise (case 2) and spanwise (cases 2 and 3) variations in pressure are much more pronounced. As a result, large parts of the wing experience an unstable mean flow for crossflow waves.

Case 2 shows relatively strong crossflow instabilities that partially lead to mixed transition (around $2y/b \approx 0.45$ and $2y/b \approx 0.9$) together with the still dominating TS waves. For case 1, the change is more severe. Transition now occurs mostly as a mix between crossflow and streamwise instabilities, where inboard TS waves still dominate transition. The change in transition mechanisms is illustrated in the $N_{\mathrm{CF}} - N_{\mathrm{TS}}$ plane for cases 1 and 4 in Fig. 20, which shows the N-factor growth for 10 different spanwise locations along the inviscid streamlines. Indeed, case 4 shows the initial growth in crossflow instabilities that does not cause transition; and then it features nearly pure TS-dominated transition. Case 1, on the other hand, is still TS dominated at the inboard sections (in blue) but features mixed transition for all other sections, except the one at $2y/b = 0.8$, where transition occurs purely due to crossflow instabilities.

It can clearly be seen from the experimental transition fronts that the transition lines of the lower two load cases have a different shape than the higher loadings. While a relatively smooth transition front

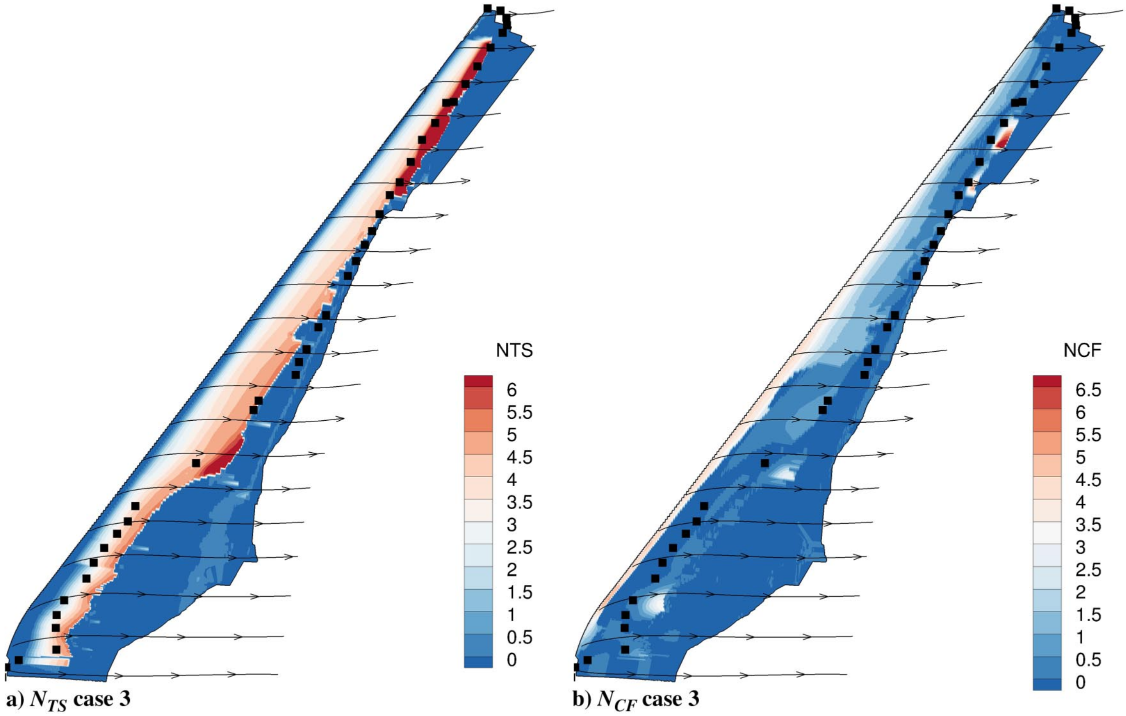

a) N_{TS} case 3 **b) N_{CF} case 3**

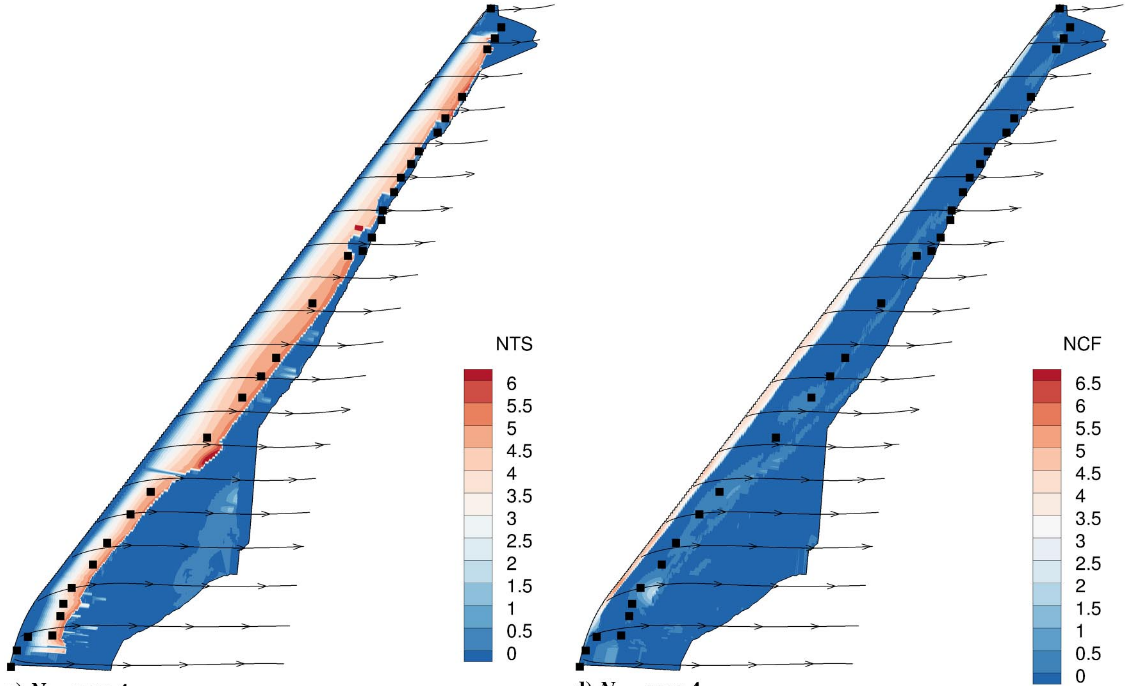

c) N_{TS} case 4 **d) N_{CF} case 4**

Fig. 19 ***N*-factor distributions on CRM-NLF with several indicated inviscid streamlines (cases 3 and 4) and transition points from experiment (black squares).**

can be observed at the two higher angles of attack, the lower two angles result in distinct kinks in the transition front (around $2y/b \approx 0.75$ for case 1 and $2y/b \approx 0.85$ for case 2). The reason can once more be found in the pressure distributions showing a complex shock pattern on the wing for the smaller angles of attack. Figure 21 shows the pressure gradient contours for cases 1 and 4 to better visualize the effect of the shocks on transition. A complex shock pattern consisting of four distinct shocks, partially overlapping in spanwise direction, are characteristic for the lower angles of attack. For case 1, the first shock extends from the wing root to about 67% of the span. Downstream of that, a second shock extends from the kink up to 95% of the span. From 85 to 98% span, a third shock is located further downstream. Lastly, a small fourth shock is observable, ranging from 95% to the leading edge of the wing tip. In contrast, the higher angles of attack result in the aforementioned pressure plateaus, with a single dominating shock ranging over the entire span located at $x/c \approx 0.75$ between at the root and the kink and shifting upstream to $x/c \approx 0.5$ outboard of the kink. Figures 18 and 20 indicate that the strong

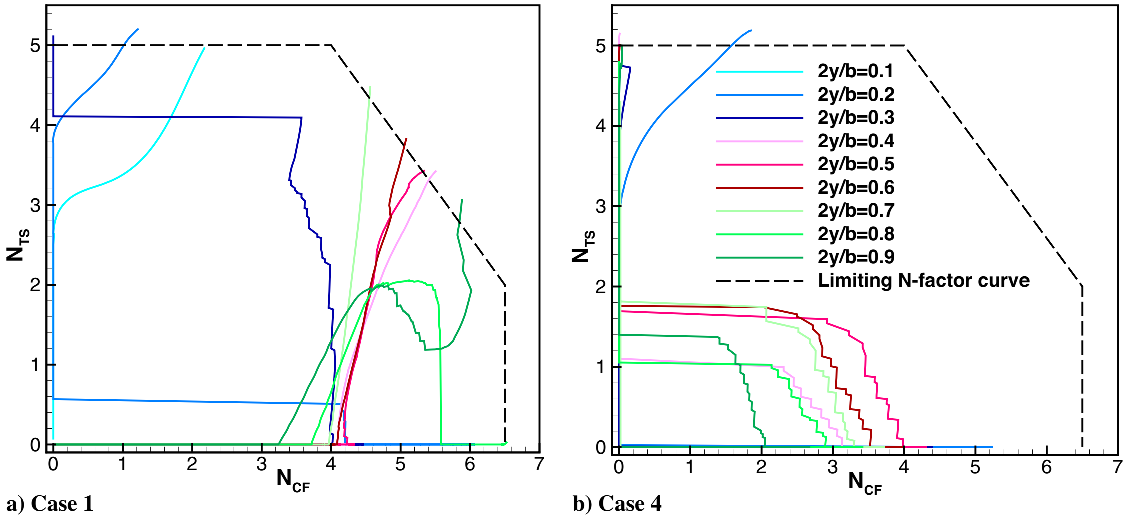

a) Case 1 b) Case 4

Fig. 20 *N*-factor development until transition for several inviscid streamlines (CRM-NLF cases 1 and 4) with indicated limiting *N*-factor curve.

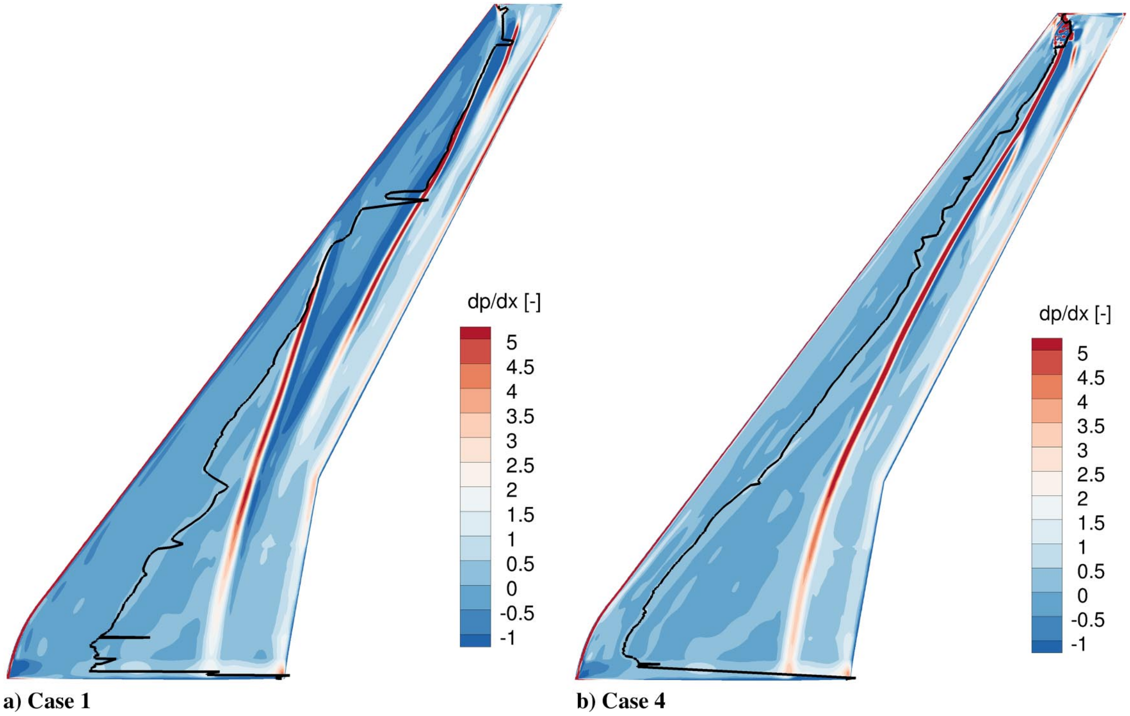

a) Case 1 b) Case 4

Fig. 21 Contour plots of the pressure gradient with respect to x on CRM-NLF with indicated numerical transition locations from LST (black lines).

spanwise change in pressure promotes crossflow instability growth that, combined with the adverse pressure gradient, leads to mixed transition shortly upstream of the shock.

Figure 22 finally shows the skin-friction coefficient contours for all four load cases with indicated experimental transition locations to compare numerical and experimental transition fronts. These are not shown as lines because the experimental visualizations contain significant areas of bypass transition. On the scaled wind-tunnel model, the slightest surface imperfections can lead to strong perturbations that locally cause bypass transition. These transition areas feature wedges that grow in the spanwise direction downstream from the leading edge such that natural transition locations are hidden downstream in some areas. Especially if the wedges merge, a large data gap exists as in the kink region of case 2.

For all cases, a good qualitative agreement exists between experimental and computed transition lines. The correctly deflected wing shape for case 4 shows an especially close resemblance. Only three areas show slight misalignment of the two transition fronts for the other cases. First, the curved transition line at the tip region is neatly followed by the prediction and follows the experimental trends, except for cases 2 and 3, where premature transition is found.

Second, the spanwise jumps for cases 1 and 2 are followed, albeit a small spanwise misalignment can be noticed. It is believed that this is a direct effect of the wrong shock location due to the mismatch in wing deflection. A publication on the experimental results by Lynde et al. [44] shows transition fronts for different dynamic pressures but the same Reynolds and Mach numbers. The presented difference in spanwise location of the transition jump amounts to roughly 3% of the semispan and closely resembles the difference found in the simulations presented in this paper. It can be concluded that the found misalignment is a possible cause of the model deflection. The smaller error of the more closely deflected case 2 supports this hypothesis.

Finally, because the turbulent boundary layer of the fuselage was not forced upon the wing surface in the current simulations, the wing–body junction area is not turbulent as in the experiment. This can be modeled if required in future analyses. It was not taken

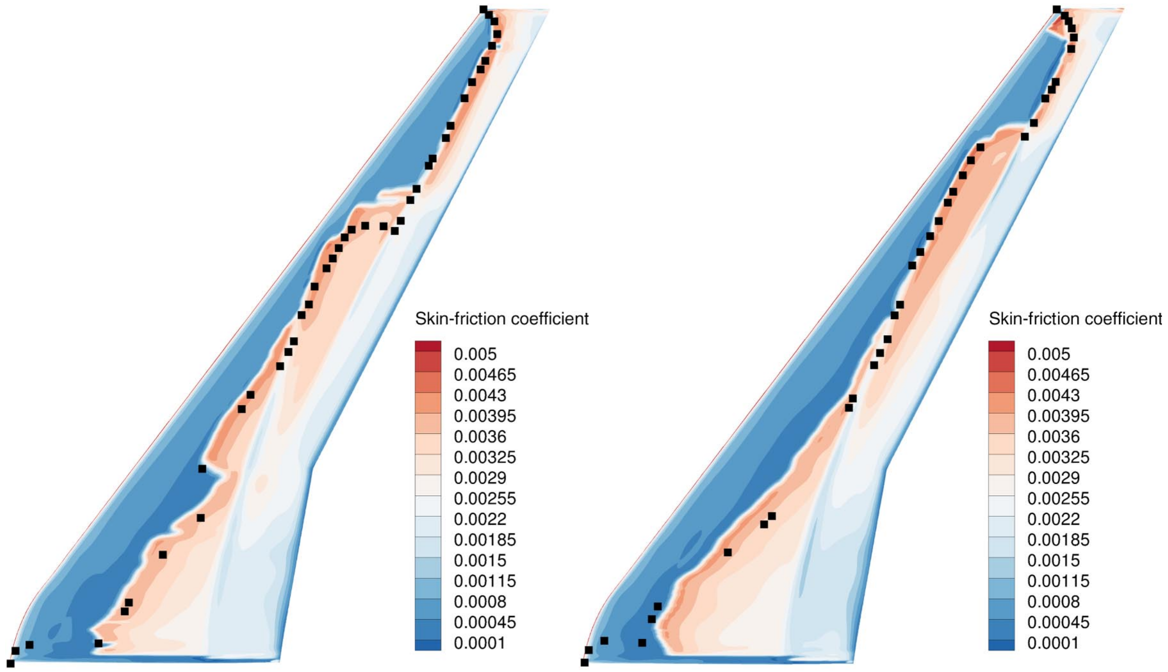

a) Case 1 **b) Case 2**

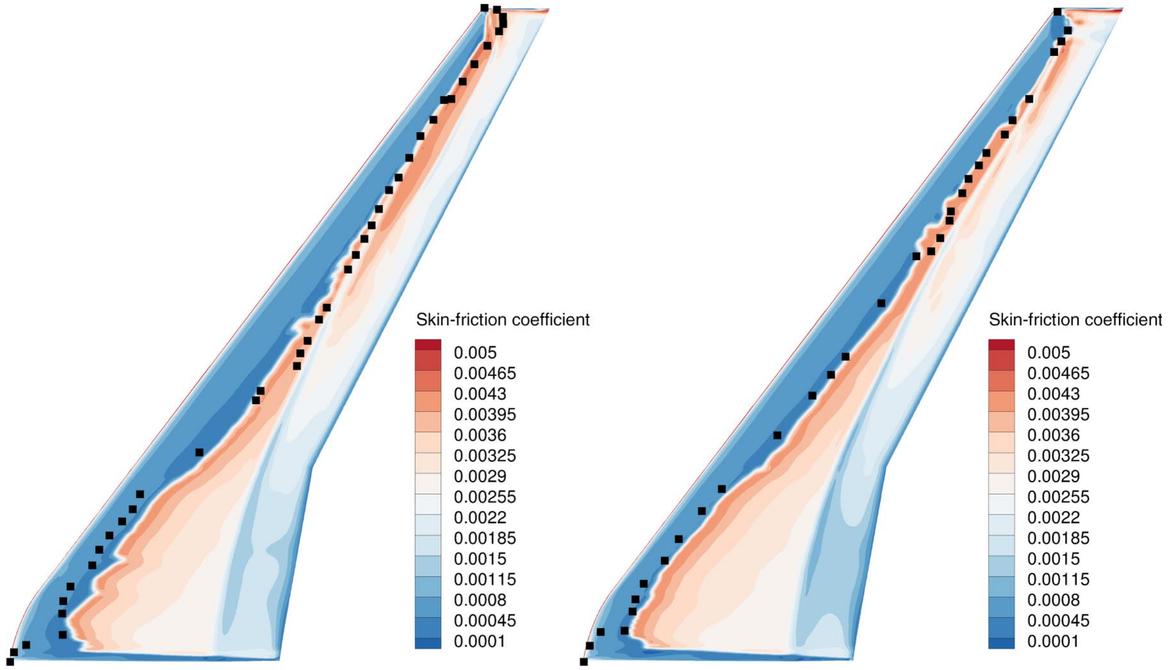

c) Case 3 **d) Case 4**

Fig. 22 Skin-friction coefficient contour on CRM-NLF upper surface for cases 1, 2, 3, and 4 resulting from RANS–LST coupling and indicated transition points from experiment (black squares).

into account in this study because the purpose was to identify natural transition locations on the wing only.

Overall, the differences between the computations and the experiment mostly fall within the experimental uncertainties in the transition fronts that are expected from Ref. [44], stemming from the visualization technique and the geometrical differences due to the flexibility of the model.

VI. Conclusions

A methodology to simulate transitional flows over wings has been presented. The NLR's ENSOLV RANS flow solver was directly coupled to the LST code COSALX. A two-N-factor approach for streamwise Tollmien–Schlichting and stationary crossflow instabilities relevant to high Reynolds numbers and low freestream turbulence environments was used. The amplification factors are integrated along inviscid streamlines on the geometry using boundary-layer profiles from the flowfield variables provided by the flow computation. Additionally, laminar separation bubbles can be captured by the LST analysis or are modeled using a shape-factor criterion for separation and a correlation for the separation-induced transition length in case LST fails to find a transition location.

The coupled simulation can be performed without user intervention. Compared to a standard fully turbulent simulation, it needs only a little more effort in the preprocessing stage; whereas it requires roughly 10 times more computational effort due to the finer grid, the additional LST computations, and the iterative coupling procedure. All this makes it suitable for the analysis of industrially relevant flows in a design process.

The TU Braunschweig sickle wing and NASA's CRM-NLF experiments have been reproduced using the established methodology. The good agreement showcases the capability of the method to deal with complex flows featuring varying and mixing paths to transition. Furthermore, new insights on the transition modes on the two validation cases were obtained by investigating the LST results. Limitations of the methodology are discussed where the coupled simulations fail to predict accurate transition locations. This is especially the case in areas with extreme local geometric changes like kinks in the leading edge, where assumptions of the used LST on (for example) locally parallel flow and noncurvature are violated.

For future investigations and design endeavors, a criterion for attachment-line instabilities may add important insights into another relevant transition mechanism for swept-wing flows. Additionally, influences of steps and gaps on the N factors should be integrated into the simulations, among others, to take the surface roughness into account. Although boundary-layer suction and blowing should be captured by the direct flow solver/LST coupling, this still needs to be verified using dedicated test cases.

Acknowledgments

This research was funded by the Netherlands Aerospace Centre (NLR) within the Flight Physics and Loads department. The authors would like to express their gratitude towards Martin Kruse (DLR, German Aerospace Center) for providing the test results for the sickle wing validation case. Additionally, they would like to thank Anthon de Bruin and Johan Kok (NLR) for their valuable discussions and work on the linear stability analysis code COSALX and the Navier–Stokes solver ENSOLV.

References

[1] Perraud, J., Deniau, H., and Casalis, G., "Overview of Transition Prediction Tools in the elsA Software," *Proceedings of the Jointly Organized 11th World Congress on Computational Mechanics—WCCM XI, 5th European Conference on Computational Mechanics—ECCM V, 6th European Conference on Computational Fluid Dynamics—ECFD VI*, edited by E. Oñate, X. Oliver, and A. Huerta, Barcelona, 2014, pp. 1–20. https://doi.org/10.2514/6.2015-2476

[2] Langtry, R. B., Sengupta, K., Yeh, D. T., and Dorgan, A. J., "Extending the $\gamma - Re_{\theta t}$ Local Correlation Based Transition Model for Crossflow Effects," AIAA Paper 2015-2474, 2015. https://doi.org/10.2514/6.2015-2474

[3] Krumbein, A., "e^N Transition Prediction for 3D Wing Configurations Using Database Methods and a Local, Linear Stability Code," *Aerospace Science and Technology*, Vol. 12, No. 8, 2008, pp. 592–598. https://doi.org/10.1016/j.ast.2008.01.005

[4] Denison, M., and Pulliam, T. H., "Implementation and Assessment of the Amplification Factor Transport Laminar-Turbulent Transition Model," AIAA Paper 2018-3382, 2018. https://doi.org/10.2514/6.2018-3382

[5] Krumbein, A., Krimmelbein, N., and Grabe, C., "Streamline-Based Transition Prediction Techniques in an Unstructured Computational Fluid Dynamics Code," *AIAA Journal*, Vol. 55, No. 5, 2017, pp. 1548–1564. https://doi.org/10.2514/1.J054990

[6] Krimmelbein, N., and Radespiel, R., "Transition Prediction for Three-Dimensional Flows Using Parallel Computation," *Computers and Fluids*, Vol. 38, No. 1, 2009, pp. 121–136. https://doi.org/10.1016/j.compfluid.2008.01.004

[7] Krumbein, A., Krimmelbein, N., and Schrauf, G., "Automatic Transition Prediction in a Hybrid Flow Solver—Part 1: Methodology and Sensitivities," *Journal of Aircraft*, Vol. 46, No. 4, 2009, pp. 1176–1190. https://doi.org/10.2514/1.39736

[8] Krumbein, A., Krimmelbein, N., and Schrauf, G., "Automatic Transition Prediction in a Hybrid Flow Solver—Part 2: Practical Application," *Journal of Aircraft*, Vol. 46, No. 4, 2009, pp. 1191–1199. https://doi.org/10.2514/1.39738

[9] Shi, Y., Gross, R., Mader, C. A., and Martins, J. R. R. A., "Transition Prediction Based on Linear Stability Theory with the RANS Solver for Three-Dimensional Configurations," AIAA Paper 2018-0819, 2018. https://doi.org/10.2514/6.2018-0819

[10] Campbell, R. L., and Lynde, M. N., "Building a Practical Natural Laminar Flow Design Capability," AIAA Paper 2017-3059, 2017. https://doi.org/10.2514/6.2017-3059

[11] Kosarev, L., Séror, S., and Lifshitz, Y., "Parabolized Stability Equations Code with Automatic Inflow for Swept Wing Transition Analysis," *Journal of Aircraft*, Vol. 53, No. 6, 2016, pp. 1647–1669. https://doi.org/10.2514/1.C033509

[12] van Ingen, J. L., "A Suggested Semi-Empirical Method for the Calculation of the Boundary Layer Transition Region," Faculty of Aerospace Engineering, Delft Univ. of Technology TR VTH-74, Delft, The Netherlands, Sept. 1956.

[13] Smith, A. M. O., and Gamberoni, N., "Transition, Pressure Gradient and Stability Theory," Engineering Dept., Douglas Aircraft Company TR ES 26388, El Segundo, CA, Aug. 1956.

[14] Kok, J. C., "A High-Order Low-Dispersion Symmetry-Preserving Finite-Volume Method for Compressible Flow on Curvilinear Grids," *Journal of Computational Physics*, Vol. 228, No. 18, 2009, pp. 6811–6832. https://doi.org/10.1016/j.jcp.2009.06.015

[15] Laban, M., Kok, J. C., and Prananta, B. B., "Numerical Tools for Contra-Rotating Open-Rotor Performance, Noise and Vibration Assessment," *Proceedings of ICAS*, Paper ICAS2010-4.2.2, 2010, pp. 1–9.

[16] Jameson, A., "A Non-Oscillatory Shock Capturing Scheme Using Flux Limited Dissipation," Large Scale Computations in Fluid Mechanics, Lectures in Applied Mathematics, Vol. 22, edited by B. E. Engquist, S. Osher, and R. C. J. Somerville, American Mathematical Soc., Providence, RI, 1985, pp. 345–370.

[17] Jameson, A., "Multigrid Algorithms for Compressible Flow Calculations," *Proceedings of the 2nd European Conference on Multigrid Methods*, edited by W. Hackbusch, and U. Trottenberg, Vol. 1228, Lectures in Applied Mathematics, Springer-Verlag, New York, 1986, pp. 166–201. https://doi.org/10.1007/BFb0072647

[18] Dol, H. S., Kok, J. C., and Oskam, B., "Turbulence Modelling for Leading-Edge Vortex Flows," AIAA Paper 2002-0843, 2002. https://doi.org/10.2514/6.2002-843

[19] Kok, J. C., "Resolving the Dependence on Freestream Values for the $k - \omega$ Turbulence Model," *AIAA Journal*, Vol. 38, No. 7, 2000, pp. 1292–1295. https://doi.org/10.2514/2.1101

[20] Walker, G. J., "Transitional Flow on Axial Turbomachine Blading," *AIAA Journal*, Vol. 27, No. 5, 1989, pp. 595–602. https://doi.org/10.2514/3.10150

[21] Arnal, D., Casalis, G., and Houdeville, R., "Practical Transition Prediction Methods: Subsonic and Transonic Flows," NATO Research & Technology Organisation (RTO), Educational Notes, EN-AVT-151, June 2008.

[22] Mack, L. M., "Boundary-Layer Linear Stability Theory," AGARD-VKI Special Course on Transition and Stability of Laminar Flow, AGARD Rept. 709, Neuilly-Sur-Seine, France, 1984.

[23] Arnal, D., "Boundary Layer Transition: Prediction Based on Linear Theory," Special Course on Progress in Transition Modelling, AGARD Rept. 793, Neuilly-Sur-Seine, France, April 1994.

[24] Saric, W. S., Reed, H. L., and White, E. B., "Stability and Transition of Three-Dimensional Boundary Layers," *Annual Review of Fluid Mechanics*, Vol. 35, No. 1, 2003, pp. 413–440. https://doi.org/10.1146/annurev.fluid.35.101101.161045

[25] de Bruin, A. C., "User's Manual for COSALX—A Method for Linear Stability Analysis of 3D Compressible Boundary Layers," Netherlands Aerospace Centre/NLR TR 90130 U, Amsterdam, April 1990.

[26] Malik, M. R., "COSAL: A Black-Box Compressible Stability Analysis Code for Transition Prediction in Three-Dimensional Boundary Layers," NASA CR-165925, May 1982.

[27] Malik, M. R., and Orszag, S. A., "Efficient Computation of the Stability of Three-Dimensional Compressible Boundary Layers," AIAA Paper 1981-1277, 1981. https://doi.org/10.2514/6.1981-1277

[28] Gaster, M., "A Note on the Relation Between Temporally-Increasing and Spatially Increasing Disturbances in Hydrodynamic Stability," *Journal of Fluid Mechanics*, Vol. 14, No. 2, 1962, pp. 222–224. https://doi.org/10.1017/S0022112062001184

[29] Krumbein, A., Krimmelbein, N., Grabe, C., and Shengyang, N., "Development and Application of Transition Prediction Techniques in an Unstructured CFD Code (Invited)," AIAA Paper 2015-2476, 2015. https://doi.org/10.2514/6.2015-2476

[30] Arnal, D., "Laminar-Turbulent Transition Prediction in Three-Dimensional Flows," *Progress in Aerospace Sciences*, Vol. 36, No. 2, 2000, pp. 173–191. https://doi.org/10.1016/S0376-0421(00)00002-6

[31] Somers, D., "Subsonic Natural-Laminar-Flow Airfoils," *Natural Laminar Flow and Laminar Flow Control*, edited by R. W. Barnwell, and M. Y. Hussaini, ICASE/NASA LaRC Series, Springer-Verlag, New York, 1992, p. 163. https://doi.org/10.1007/978-1-4612-2872-1_4

[32] Knopp, T., and Probst, A., "An Algebraic Sensor for the RANS-LES Switch in Delayed Detached-Eddy Simulation," *New Results in Numerical and Experimental Fluid Mechanics VIII, Notes on Numerical Fluid Mechanics and Multidisciplinary Design*, edited by A. Dillmann, G. Heller, H.-P. Kreplin, W. Nietsche, and I. Peltzer, Springer-Verlag, Berlin, 2013, pp. 461–462.

[33] Roberts, W. B., "Calculation of Laminar Separation Bubbles and Their Effect on Airfoil Performance," *AIAA Journal*, Vol. 18, No. 1, 1980, pp. 25–31. https://doi.org/10.2514/3.50726

[34] Bernardos, L., Richez, F., Gleize, V., and Gerolymos, A., "Algebraic Nonlocal Transition Modeling of Laminar Separation Bubbles Using $k-\omega$ Turbulence Models," *AIAA Journal*, Vol. 57, No. 2, 2019, pp. 553–565. https://doi.org/10.2514/1.J057734

[35] Nebel, C., Radespiel, R., and Wolf, T., "Transition Prediction for 3D Flows Using a Reynolds-Averaged Navier–Stokes Code and N-Factor Methods," AIAA Paper 2003-3593, 2003. https://doi.org/10.2514/6.2003-3593

[36] Krumbein, A., "Automatic Transition Prediction for High-Lift Systems Using a Hybrid Flow Solver," *Journal of Aircraft*, Vol. 42, No. 5, 2005, pp. 1362–1366. https://doi.org/10.2514/1.16173

[37] Reed, H. L., and Saric, W. S., "CFD Validation Issues for Boundary-Layer Stability and Transition," AIAA Paper 2003-3441, 2003. https://doi.org/10.2514/6.2003-3441

[38] Baldwin, B., and Lomax, H., "Thin-Layer Approximation and Algebraic Model for Separated Turbulent Flow," AIAA Paper 1978-0257, 1978. https://doi.org/10.2514/6.1978-257

[39] Stock, J. W., and Haase, W., "Some Aspects of Linear Stability Calculations in Industrial Applications," *Transitional Boundary Layers in Aeronautics, Proceedings of the Colloquium 'Transitional Boundary Layers in Aeronautics'*, edited by R. A. W. M. Henkes, and J. L. van Ingen, Royal Netherlands Academy of Arts and Sciences, Amsterdam, 1996, pp. 225–238.

[40] Petzold, R., and Radespiel, R., "Transition on a Wing with Spanwise Varying Crossflow and Linear Stability Analysis," *AIAA Journal*, Vol. 53, No. 2, 2015, pp. 321–335. https://doi.org/10.2514/1.J053127

[41] Lynde, M. N., and Campbell, R. L., "Computational Design and Analysis of a Transonic Natural Laminar Flow Wing for a Wind Tunnel Model," AIAA Paper 2017-3058, 2017. https://doi.org/10.2514/6.2017-3058

[42] Kruse, M., Munoz, F., and Radespiel, R., "Transition Prediction Results for Sickle Wing and NLF(1)-0416 Test Cases," AIAA Paper 2018-0537, 2018. https://doi.org/10.2514/6.2018-0537

[43] Kruse, M., Küpper, A., Petzold, R., and Munoz, F., "Determination of the Critical Cross Flow N-Factor for the Low-Speed Wind Tunnel Braunschweig (DNW-NWB)," *New Results in Numerical and Experimental Fluid Mechanics XI, Notes on Numerical Fluid Mechanics and Multidisciplinary Design*, edited by A. Dillmann, G. Heller, E. Krämer, C. Wagner, S. Bansmer, R. Radespiel, and R. Semaan, Springer-Verlag, Berlin, 2018, pp. 251–261. https://doi.org/10.1007/978-3-319-64519-3_23

[44] Lynde, M. N., Campbell, R. L., and Viken, S. A., "Additional Findings from the Common Research Model Natural Laminar Flow Wind Tunnel Test," AIAA Paper 2019-3292, 2019. https://doi.org/10.2514/6.2019-3292

[45] Lynde, M. N., Campbell, R. L., Rivers, M. B., Viken, S. A., Chan, D. T., Watkins, A. N., and Goodliff, S. L., "Preliminary Results from an Experimental Assessment of a Natural Laminar Flow Design Method," AIAA Paper 2019-2298, 2019. https://doi.org/10.2514/6.2019-2298

S. Fu
Associate Editor